

Time-Domain Equivalent Circuits for the Link Modeling Between Pulsed Photoconductive Sources and Receivers

Zhang, Huasheng ; Llombart, Nuria; Bueno , Juan; Freni, Angelo

DOI

[10.1109/TTHZ.2024.3364768](https://doi.org/10.1109/TTHZ.2024.3364768)

Publication date

2024

Document Version

Final published version

Published in

IEEE Transactions on Terahertz Science and Technology

Citation (APA)

Zhang, H., Llombart, N., Bueno , J., & Freni, A. (2024). Time-Domain Equivalent Circuits for the Link Modeling Between Pulsed Photoconductive Sources and Receivers. *IEEE Transactions on Terahertz Science and Technology*, 14(3), 311-326. <https://doi.org/10.1109/TTHZ.2024.3364768>

Important note

To cite this publication, please use the final published version (if applicable). Please check the document version above.

Copyright

Other than for strictly personal use, it is not permitted to download, forward or distribute the text or part of it, without the consent of the author(s) and/or copyright holder(s), unless the work is under an open content license such as Creative Commons.

Takedown policy

Please contact us and provide details if you believe this document breaches copyrights. We will remove access to the work immediately and investigate your claim.

Green Open Access added to TU Delft Institutional Repository

'You share, we take care!' - Taverne project

<https://www.openaccess.nl/en/you-share-we-take-care>

Otherwise as indicated in the copyright section: the publisher is the copyright holder of this work and the author uses the Dutch legislation to make this work public.

Time-Domain Equivalent Circuits for the Link Modeling Between Pulsed Photoconductive Sources and Receivers

Huasheng Zhang , *Member, IEEE*, Nuria Llombart , *Fellow, IEEE*, Juan Bueno ,
Angelo Freni , *Senior Member, IEEE*, and Andrea Neto , *Fellow, IEEE*

Abstract—Photoconductive antennas (PCAs) are promising candidates for sensing and imaging applications. In recent years, our group has investigated their properties under pulsed laser illumination in transmission using a time-domain (TD) Norton equivalent circuit. Here, we extend this analysis to the link between a photoconductive source and a receiver introducing for the latter a second TD Norton equivalent circuit. We also evaluate the transfer function of a dispersive quasi-optical (QO) link. Specifically, a field correlation approach based on the high-frequency techniques is used to evaluate the spectral transfer function between two bow-tie-based PCAs, including the QO link. The detected currents in the receiving circuit are reconstructed using stroboscopic sampling of the modeled THz pulses, equivalent to what is actually performed by THz TD systems. Both the amplitude and the waveforms of these currents are evaluated. The QO link is then experimentally characterized to validate the proposed methodology. The comparison between the simulations and the measurements is excellent.

Index Terms—Bow-tie antenna (BTA), field correlation, Norton equivalent circuit, photoconductive antennas (PCAs), quasi-optical (QO) link.

I. INTRODUCTION

THE past decades have experienced increasing interest in photoconductive antennas (PCAs) for spectroscopy and imaging applications, thanks to their ability to generate and detect THz pulses when excited by pulsed optical sources [1], [2], [3], [4], [5], [6], [7]. The examples of systems, often referred to as THz time-domain (TD) systems, can be found in [8], [9], [10], [11], [12], [13], [14], [15], [16], [17], [18], and [19]. Such a system mainly consists of a photoconductive (PC) source, a PC receiver, and an in-between quasi-optical (QO) link where dielectric lenses and reflectors are commonly used to collimate and focus THz pulses.

Manuscript received 5 October 2023; revised 21 December 2023 and 23 January 2024; accepted 27 January 2024. Date of publication 12 February 2024; date of current version 3 May 2024. (Corresponding author: Huasheng Zhang.)

Huasheng Zhang, Nuria Llombart, Juan Bueno, and Andrea Neto are with the Microelectronics Department, Delft University of Technology, 2628 CD Delft, The Netherlands (e-mail: h.zhang-12@tudelft.nl; n.llombartjuan@tudelft.nl; j.buenolopez@tudelft.nl; a.neto@tudelft.nl).

Angelo Freni is with the Dipartimento di Ingegneria dell'Informazione (DINFO), Università degli Studi di Firenze, 50139 Florence, Italy (e-mail: angelo.freni@unifi.it).

Color versions of one or more figures in this article are available at <https://doi.org/10.1109/TTHZ.2024.3364768>.

Digital Object Identifier 10.1109/TTHZ.2024.3364768

For a PC source, realizing an efficient coupling between the PC material and the antenna has been one of the main challenges, especially when the objective is the maximization of the THz power radiated for a given optical power. Moving the attention to the modeling, two types of approaches have been explored for a PC source: full-wave finite-difference TD models [20], [21] and equivalent circuit models [22], [23], [24], [25], [26], [27], [28], [29], [30], [31], [32], [33]. We focus on the latter approach since it is more intuitive and convenient for designing and optimizing PCAs. Recently, the accurate TD Norton equivalent circuit based on the PC constitutive (Drude) relations combined with an electromagnetic (EM) based derivation was proposed [32]. The photocurrent flowing across the PC gap was solved in TD using a marching-on-time scheme, which accounts for the constitutive relations for low-temperature grown gallium arsenide (LTGaAs) [33].

The amplitude of the THz pulses generated by a PC source is related to the amplitude of the THz photocurrents in the PC gap [8]. The waveforms of the emitted pulses were analytically evaluated for simple antenna geometries, such as short dipoles [9]. However, if the transmitting PCA structures are more complex [18], [34], full-wave simulations need to be used to accurately model these pulses. A transfer function $H(f)$ can be introduced to characterize the QO link between PCAs [11]; but in most cases, it was approximated by the far-field link conditions, e.g., [11], [12], and [18]. In [9], the transfer function was approximately modeled by a Gaussian-beam formalism instead. However, the effect of the receiving antenna is neglected in the transfer function in all cases.

At the receiver side, the arriving THz pulses induce photocurrents in the PC gap when it is illuminated by laser pulses. The receiver can be modeled by a Thévenin equivalent circuit [11], [19], where the generator was associated with the arriving THz pulses via the approximated transfer function. The Thévenin load was evaluated using an approximated PC constitutive relation and the detected currents were evaluated using stroboscopic sampling. Since the link between PCAs has not been accurately modeled, the existing literature only compares the modeled detected currents to measurements using arbitrary units.

In this work, we first use the TD Norton equivalent circuit in [32] and [33] to analyze a PC source. We simplify the time-marching evaluation of the constitutive relations via the introduction of a generator resistance. We then characterize

the coupling between two PCAs, including the QO link, by accurately modeling the link transfer function $H(f)$ (instead of using an approximation of it). We use an EM methodology that combines full-wave simulations, physical optics (PO), and a field correlation approach [35], [36]. This procedure can be easily extended to very different link geometries since the link is studied separately from the TD analysis of PCAs. Finally, we propose a Norton equivalent circuit for the PC receiver to model the photocurrents in the PC gap. The current generator in the proposed circuit is calculated using the transfer function and the photocurrents are evaluated using the PC constitutive relation. The detected current is then reconstructed by simulating the stroboscopic sampling, which is achieved in the actual TD instruments by changing the optical delay of the laser pulses in reception (Rx). In this respect, the modeling reconstructs the sampling process performed in the commercial Menlo system [37], which is available in our laboratory. We replace the fiber-coupled PCAs [38] with our own free-space excited bow-tie PCAs [33]. These bow-tie PCAs are then coupled via two plano-convex QO lenses. The measured currents are compared with the simulations, showing excellent agreement in both waveforms and amplitude.

The rest of this article is organized as follows. Section II introduces and summarizes the TD Norton equivalent circuit for a PC source. Then, an approximate Norton generator resistance is derived to simplify the TD marching-on-time calculation. Section III describes the Norton equivalent circuit for a PC receiver to calculate the photocurrents in the PC gap. The procedure to obtain the detected currents via the stroboscopic sampling is also discussed. Section IV discusses the modeling of a dispersive QO link between two PCAs. Two bow-tie-based PCAs are used as examples to demonstrate the link transfer function and the detected currents. Section V shows the experimental characterization of the used PCAs to validate the proposed methodology. Finally, Section VI concludes this article.

II. NORTON EQUIVALENT CIRCUIT IN TRANSMISSION

We first consider the modeling of a PC gap excited in transmission (Tx) and connected to a nondispersive transmission line with the characteristic impedance of Z_0 , as depicted in Fig. 1(a). The corresponding transmission line model is shown in Fig. 1(b). By using this model, we can focus on the modeling and understanding of a PC source and receiver without including the impact of a dispersive link. This is an ideal representation since any practical implementation will include losses and dispersion. Those effects can be added via a link transfer function, as will be explained in Section IV. The transmission line is represented by two pieces of metal processed on a photosensitive semiconductor, which is biased by an external voltage source V_b . A pulsed laser with pulsewidth of τ_p illuminates the PC gap periodically with repetition time of T . Within each repetition, the laser pulse excites the electrons inside the semiconductor from their valence band to the conduction band. In response to the biasing voltage, the freed electrons form a time-varying pulsed current with very short pulsewidth (in the order of ps). Therefore, the current can radiate a pulsed field in the THz regime. The generated pulsed

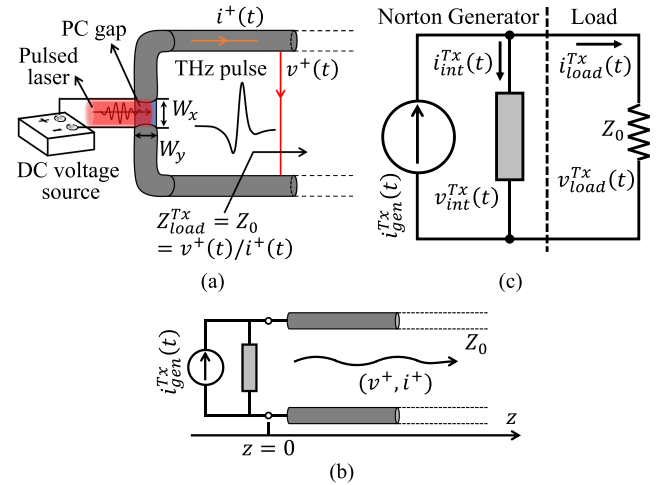


Fig. 1. (a) Schematic representation of a transmission line excited by a PC gap, which is illuminated by a pulsed laser and biased by a dc voltage source. (b) Transmission line model of (a). A pulsed THz forward wave, $[v^+(t), i^+(t)]$, is generated in the transmission line. The red line in (a) represents the biasing electric field, while the orange line is the electric current in the presence of the laser excitation. $v^+(t)$ is opposed to the biasing electric field. (c) Corresponding TD Norton equivalent circuit used to evaluate the time evolution of the THz voltage and current, $[v_{load}^{Tx}(t), i_{load}^{Tx}(t)] = [v^+(t), i^+(t)]$.

THz field propagates along this transmission line as a forward wave with the amplitude of $v^+(t)$ and $i^+(t)$, as depicted in Fig. 1(a) and (b).

By solving the transmission line in Fig. 1(b), a Norton equivalent circuit was modeled in TD [32], as shown in Fig. 1(c). This equivalent circuit is valid to model the THz voltage $v_{load}^{Tx}(t)$ and the current $i_{load}^{Tx}(t)$, in the PC gap (the Tx superscript indicates the voltage and the current are in the transmitting/source PC gap). The forward wave at $z = 0$ will then be given by the voltage and current: $v^+(t) = v_{load}^{Tx}(t)$ and $i^+(t) = i_{load}^{Tx}(t)$. This circuit was derived via a rigorous EM formulation that accounts for the constitutive (Drude) relation of the PC material. The main focus is on modeling the THz photocurrents on the external load branch. Here, we assume the external load as a resistance; thus, we only consider the first-order effect of the load, which corresponds to its radiation, as explained in [32] and [33]. More complex modeling of a PC source has been discussed in several works, e.g., [28] and [29], where different mechanisms were considered. In this work, we use the equivalent Norton circuit since it imposes the continuity of currents that fits best with the voltage-to-current constitutive Drude relation [32]. For the sake of completeness, the current components of the Norton circuit are summarized as follows.

- 1) The generator current $i_{gen}^{Tx}(t)$ is the impressed current by the laser under a short-circuited gap condition, with a constant biasing voltage V_b . The current was explicitly derived in [33] and it can be expressed as the PC constitutive relation shown as follows:

$$i_{gen}^{Tx}(t) = \frac{q_e^2}{m_e} \frac{W_y W_z}{W_x} \int_{t_0}^t n_p^{Tx}(t, t'') \int_{t''}^t e^{-\frac{t-t'}{\tau_s^{Tx}}} V_b dt' dt'' \quad (1)$$

where q_e is the electron charge and m_e is the effective mass of the electrons in the PC material; W_x , W_y , and W_z are the dimensions of the PC gap; t_0 is the laser arrival time; and τ_s^{Tx} is the scattering time of the PC material. $n_p^{Tx}(t, t')$ is the carrier density generation rate [unit $1/(m^3s)$]. It represents the average number of electrons in the PC gap volume remaining at time t after being excited at time t' , and it is expressed as follows:

$$n_p^{Tx}(t, t') = \frac{\eta_{\text{gen}}^{Tx}}{W_x W_y W_z} \frac{\tilde{P}_{\text{opt}}^{Tx}}{h f_c} \frac{T}{\tau_p} \sqrt{\frac{4 \ln 2}{\pi}} e^{-4 \ln 2 \left(\frac{t-t'}{\tau_p}\right)^2} e^{-\frac{t-t'}{\tau_c^{Tx}}}. \quad (2)$$

Here, h is the Planck constant, f_c is the laser operation frequency, and $\tilde{P}_{\text{opt}}^{Tx}$ is the average optical power of the laser interacting with the PC gap, which considers the spillover of the laser beam on the PC gap and the absorption efficiency of the semiconductor. We introduce here an efficiency term, η_{gen}^{Tx} (generation efficiency), to account for the effects (losses), which are not modeled in the current formalism.

- 2) The internal current $i_{\text{int}}^{Tx}(t)$ is the current flowing on the generator load branch. It ensures that the time-varying THz voltage $v_{\text{int}}^{Tx}(t) = v_{\text{load}}^{Tx}(t)$ verifies the constitutive relation. It can be evaluated as follows:

$$i_{\text{int}}^{Tx}(t) = \frac{q_e^2}{m_e} \frac{W_y W_z}{W_x} \int_{t_0}^t n_p^{Tx}(t, t') \int_{t''}^t e^{-\frac{t-t'}{\tau_s^{Tx}}} v_{\text{int}}^{Tx}(t') dt' dt''. \quad (3)$$

Note that this expression is the same as (1) except V_b is replaced by $v_{\text{int}}^{Tx}(t)$.

- 3) The load current $i_{\text{load}}^{Tx}(t)$ represents the THz current flowing across the external load. It is, thus, associated with the THz radiation. The constitutive relation in this branch is given by the transmission line in Fig. 1(b). Assuming an infinite line, the load impedance seen from the generator will correspond to the transmission line characteristic impedance, Z_0 . Then, the voltage-to-current relation is $i_{\text{load}}^{Tx}(t) = v_{\text{load}}^{Tx}(t)/Z_0$, which is purely real.

The relations in (1) and (3) are nonlinear as they depend on the laser excitation starting at t_0 . Accordingly, a marching-on-time scheme was implemented to solve the time evolution of $v_{\text{load}}^{Tx}(t)$ and $i_{\text{load}}^{Tx}(t)$, as discussed in [33]. This method discretizes the currents and voltages involved in time and solves them progressively using the previously discussed constitutive relations. Once the time evolutions of $v_{\text{load}}^{Tx}(t)$ and $i_{\text{load}}^{Tx}(t)$ are found, the instantaneous power delivered to the load or carried by the THz forward wave in the present example can be calculated as $p_{\text{load}}^{Tx}(t) = i_{\text{load}}^{Tx}(t)v_{\text{load}}^{Tx}(t)$. The average THz power over the laser repetition time is then

$$\tilde{P}_{\text{load}}^{Tx} = \frac{1}{T} \int_0^T p_{\text{load}}^{Tx}(t) dt. \quad (4)$$

A. Example Solutions of the Circuit

An example of the solved currents and voltages is shown in Fig. 2. Here, we consider LT GaAs ($\epsilon_r = 12.94$) as the PC material, with a typical gap volume of $10 \mu\text{m} \times 10 \mu\text{m} \times 2 \mu\text{m}$,

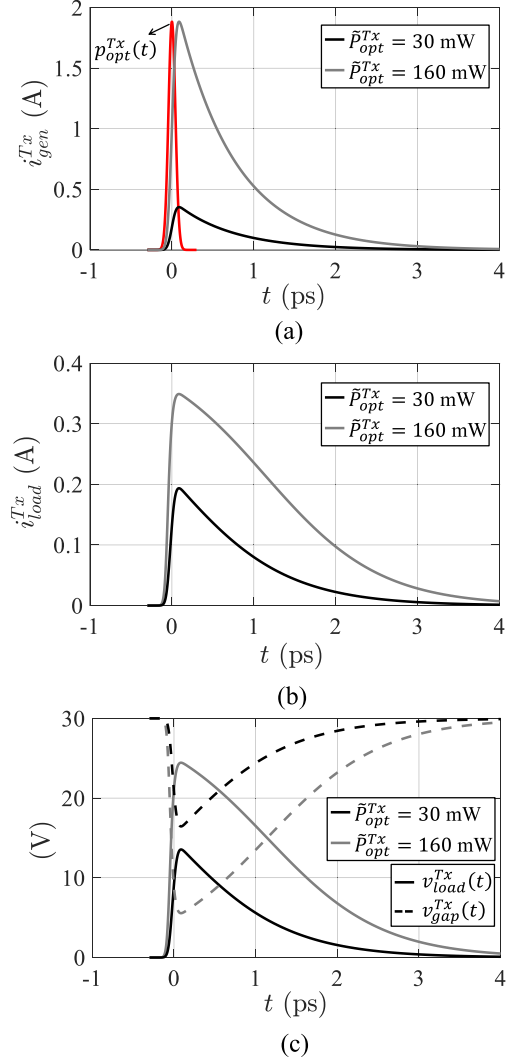


Fig. 2. (a) Norton generator current $i_{\text{gen}}^{Tx}(t)$. The laser pulse is also shown with its amplitude normalized to that of $i_{\text{gen}}^{Tx}(t)$. (b) Time-varying current $i_{\text{load}}^{Tx}(t)$ on the external load. (c) Corresponding time-varying voltage $v_{\text{load}}^{Tx}(t)$ on the load. The gap voltage $v_{\text{gap}}^{Tx}(t) = V_b - v_{\text{load}}^{Tx}(t)$ is also shown. Here, we consider two optical power levels: $\tilde{P}_{\text{opt}}^{Tx} = 30$ mW and 160 mW. The biasing voltage is $V_b = 30$ V and the load impedance is $Z_0 = 70 \Omega$. $\tau_c^{Tx} = 700$ fs, $\tau_s^{Tx} = 8.5$ fs, and $\eta_{\text{gen}}^{Tx} = 25.6\%$.

biased by $V_b = 30$ V. The material is characterized by the scattering and recombination time of $\tau_s^{Tx} = 8.5$ fs and $\tau_c^{Tx} = 700$ fs, respectively, and the generation efficiency is $\eta_{\text{gen}}^{Tx} = 25.6\%$. The transmission line impedance is assumed as $Z_0 = 70 \Omega$. The pulsed laser operates at $f_c = 384.6$ THz (wavelength of 780 nm) and its time evolution has a Gaussian shape with the full width at half maximum (FWHM) duration of $\tau_p = 100$ fs and the repetition time of $T = 12.5$ ns. The spatial distribution of the laser is also Gaussian, which is truncated on the PC gap with the FWHM beam width of $10 \mu\text{m}$. Such truncation is quantified by the spillover efficiency of the laser beam on the gap. By also considering the absorption efficiency of the semiconductor, the average optical power absorbed by the gap is $\tilde{P}_{\text{opt}}^{Tx} = 30$ mW. These parameters are relevant for the measurements that will be

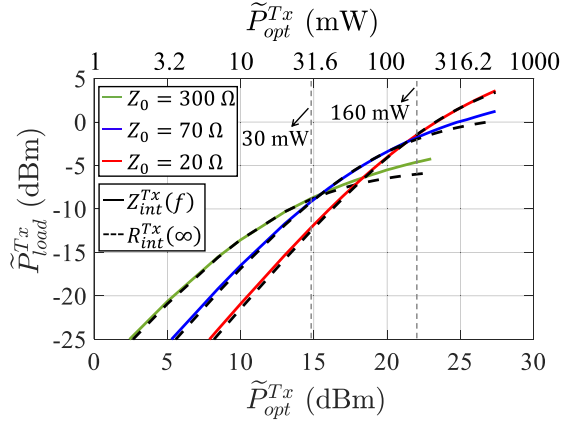


Fig. 3. Power delivered to the load \tilde{P}_{load}^{Tx} versus the laser optical power on the gap \tilde{P}_{opt}^{Tx} , when $V_b = 30$ V for different loading conditions. The solid curves correspond to the results of the time-marching solution of the constitutive relations; whereas the dotted curves correspond to the results calculated using the analytical generator resistance $R_{int}^{Tx}(\infty)$.

discussed in Section V. In Fig. 2(a), when a laser pulse arrives, the generator current $i_{gen}^{Tx}(t)$ starts to increase and then it gradually drops due to the recombination process. The time-varying THz current $i_{load}^{Tx}(t)$ in Fig. 2(b) shows the same behavior as $i_{gen}^{Tx}(t)$ and its waveform is similar to that of $i_{gen}^{Tx}(t)$. In Fig. 2(c), the time-varying voltage $v_{load}^{Tx}(t)$ behaves similarly to $i_{load}^{Tx}(t)$ and its amplitude is $i_{load}^{Tx}(t)Z_0$. This voltage is opposite to the biasing voltage (due to the movement of the free electrons). Therefore, the net voltage on the PC gap is $v_{gap}^{Tx}(t) = V_b - v_{load}^{Tx}(t)$, which is also shown in the figure. Note that $v_{gap}^{Tx}(t)$ is not the output voltage in the circuit since the proposed Norton circuit does not model the dc components [32]. In the same figure, an example with much higher optical power, $\tilde{P}_{opt}^{Tx} = 160$ mW, is also shown. It can be observed that the amplitude of $i_{gen}^{Tx}(t)$ is proportional to \tilde{P}_{opt}^{Tx} and its waveform remains the same. The amplitude of $i_{load}^{Tx}(t)$ and $v_{load}^{Tx}(t)$ also increases as \tilde{P}_{opt}^{Tx} increases; however, their waveforms start to get distorted when \tilde{P}_{opt}^{Tx} is very high and $v_{gap}^{Tx}(t)$ almost reaches the zero value. This effect is related to the saturation of the THz power \tilde{P}_{load}^{Tx} being generated.

Fig. 3 shows the power delivered to the transmission line, \tilde{P}_{load}^{Tx} (solid curves), versus the laser optical power, \tilde{P}_{opt}^{Tx} . We observe that when \tilde{P}_{opt}^{Tx} is high, $\tilde{P}_{load}^{Tx}(Z_0 = 70 \Omega)$ starts to saturate. This effect can be well explained by the used Norton equivalent circuit in terms of the impedance matching. If we apply the Fourier transform (FT) on the TD current and voltage (within one laser repetition time) in the generator load branch from Fig. 1(c), we obtain their frequency representation: $I_{int}^{Tx}(f)$ and $V_{load}^{Tx}(f) = V_{int}^{Tx}(f)$. We can then evaluate the internal generator impedance as $Z_{int}^{Tx}(f) = V_{int}^{Tx}(f)/I_{int}^{Tx}(f)$. This impedance is shown in Fig. 4 for the same case used in Fig. 2. When the laser optical power \tilde{P}_{opt}^{Tx} is low [see Fig. 4(a)], $\text{Real}[Z_{int}^{Tx}(f)]$ is comparable to Z_0 (70Ω). Thus, for low power levels, \tilde{P}_{load}^{Tx} increases linearly in the scale, as shown in Fig. 3. As \tilde{P}_{opt}^{Tx} increases to 160 mW, as shown in Fig. 4(b), $Z_{int}^{Tx}(f)$ drops significantly and $\text{Real}[Z_{int}^{Tx}(f)] < Z_0$. Thus, Z_0 cannot match

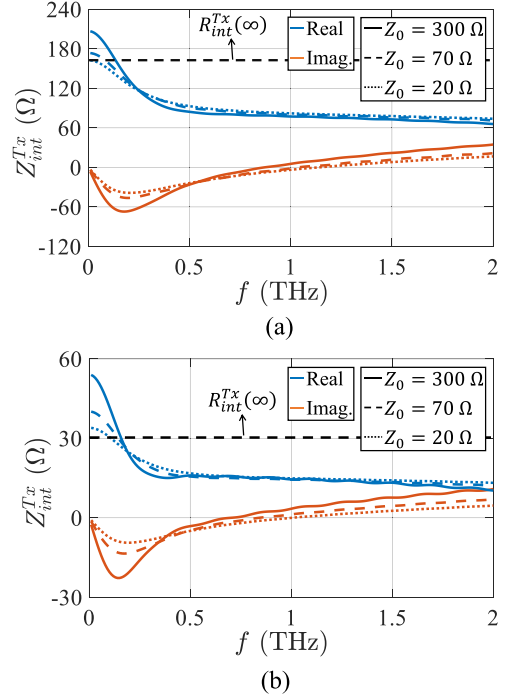


Fig. 4. Norton generator impedance $Z_{int}^{Tx}(f)$ when three values of the load impedance are used: $Z_0 = 20 \Omega$, 70Ω , and 300Ω . The optical power \tilde{P}_{opt}^{Tx} is (a) 30 mW and (b) 160 mW. The biasing voltage is $V_b = 30$ V. In the same figures, the analytical generator resistance $R_{int}^{Tx}(\infty)$ calculated using (5) is also plotted for reference.

with $Z_{int}^{Tx}(f)$ and $\tilde{P}_{load}^{Tx}(Z_0 = 70 \Omega)$ does not follow the same linear growth in Fig. 3.

We have also calculated $Z_{int}^{Tx}(f)$ for the other two different values of Z_0 : 20Ω and 300Ω , plotted also in Fig. 4. For very low Z_0 , since it is always lower or comparable to $Z_{int}^{Tx}(f)$ below $\tilde{P}_{opt}^{Tx} = 160$ mW, \tilde{P}_{load}^{Tx} does not show any power saturation (see the red solid curve in Fig. 3). On the other hand, for very high Z_0 , it cannot match with $Z_{int}^{Tx}(f)$ even at low power level, as shown in Fig. 4(a). Thus, \tilde{P}_{load}^{Tx} is already saturated at $\tilde{P}_{opt}^{Tx} = 30$ mW, as shown by the green curve in Fig. 3. Therefore, the impedance matching is directly associated with the power saturation and should be considered when designing the load impedance Z_0 . In our laboratory system, \tilde{P}_{opt}^{Tx} has a limit of 80 mW; therefore, we design the PCA with an impedance close to 70Ω to achieve the optimal delivered power between 0 and 80 mW. To achieve such an optimal design, one must use the marching-on-time method to iteratively calculate $Z_{int}^{Tx}(f)$ for different \tilde{P}_{opt}^{Tx} and Z_0 until the best impedance matching is achieved. Unfortunately, such a process is time-consuming and not intuitive.

B. Norton Resistance

To better consider the impedance matching and simplify the numerical time-marching evaluation of the TD Norton circuit, we show in Appendix A how $Z_{int}^{Tx}(f)$ can be approximated by a resistance $R_{int}^{Tx}(Z_0)$, which was also discussed in [39]. This resistance can be assumed to be independent of the load, so we indicate it as $R_{int}^{Tx}(\infty)$. It can be directly calculated with the

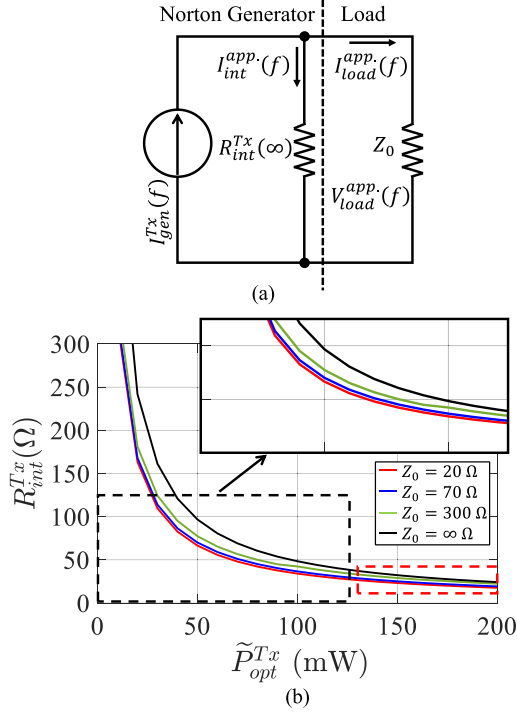


Fig. 5. (a) Proposed FD Norton equivalent circuit with constant generator resistance $R_{int}^{Tx}(\infty)$ calculated using (5). (b) $R_{int}^{Tx}(\infty)$ versus \tilde{P}_{opt}^{Tx} . Numerical solution of $R_{int}^{Tx}(Z_0)$ calculated using (A.2) is also shown for comparison. We consider $Z_0 = 20 \Omega$, 70Ω , and 300Ω . The dashed red box indicates the power saturation region.

parameters of the laser source, the PC material, and the gap size as follows:

$$R_{int}^{Tx}(\infty) = \frac{2hf_c W_x^2}{\mu_{dc}^{Tx} q_e T \eta_{gen}^{Tx} \tilde{P}_{opt}^{Tx}} \frac{\tau_c^{Tx} + \tau_s^{Tx}}{\tau_c^{Tx} - \tau_s^{Tx}} \quad (5)$$

where $\mu_{dc}^{Tx} = \tau_s^{Tx} q_e / m_e$ is the dc mobility of the PC material. The use of this resistance simplifies the evaluation of the PC constitutive relation and introduces a Norton equivalent circuit in frequency domain (FD), as shown in Fig. 5(a). The notations of the currents and the voltage have the additional *app.* superscripts indicating that they have been approximated. Since the generator's current $I_{gen}^{Tx}(f)$ can also be analytically calculated, as discussed in [31], the whole circuit in Fig. 5(a) can be solved analytically without any time-marching evaluation.

This resistance is plotted in Fig. 5(b) by the black curve. In addition, we calculate $R_{int}^{Tx}(Z_0)$ numerically using (A.2) with the time-marching method and it is plotted versus different Z_0 for comparison. We can notice that $R_{int}^{Tx}(\infty)$ is close to the numerical evaluation of $R_{int}^{Tx}(Z_0 = 300 \Omega)$. Moreover, as \tilde{P}_{opt}^{Tx} increases, $R_{int}^{Tx}(\infty)$ tends to converge to a constant, which indicates power saturation via impedance mismatched to a load. Therefore, we should design our load before the saturation region, as shown by the dashed red box in Fig. 5(b). In the case of $Z_0 = 70 \Omega$, the impedance-matched condition can be fulfilled when $\tilde{P}_{opt}^{Tx} \approx 50$ mW, which is before the saturation, as shown in Fig. 3.

To evaluate the applicability of the circuit in Fig. 5(a), we can calculate the THz power generated in the load and compare it

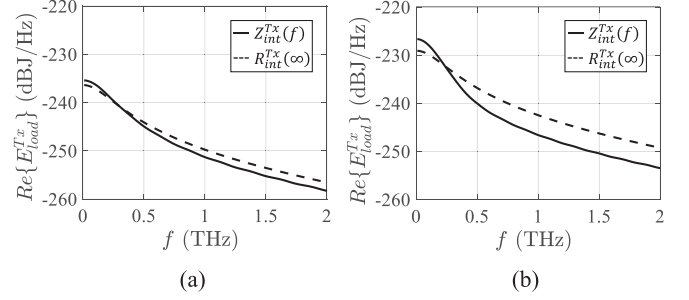


Fig. 6. Energy spectral density of the load when \tilde{P}_{opt}^{Tx} is (a) 30 mW and (b) 160 mW, $V_b = 30$ V, and $Z_0 = 70 \Omega$. The results are evaluated using the Norton circuits in Tx in Figs. 1(c) and 5(a).

with the numerical results (time-marching results) in Fig. 3. As expected, the agreement is excellent before the power saturation. This is because \tilde{P}_{load}^{Tx} is highly dominated by the low-frequency components where $Z_{int}^{Tx}(f)$ is comparable to $R_{int}^{Tx}(\infty)$, as shown in Fig. 4. However, when \tilde{P}_{opt}^{Tx} increases to the level where saturation occurs and Z_0 is high, it becomes more inaccurate to approximate $Z_{int}^{Tx}(f)$ by $R_{int}^{Tx}(\infty)$. As the result, the numerical evaluation of $\tilde{P}_{load}^{Tx}(Z_0 = 300 \Omega)$ in Fig. 3 is higher for high \tilde{P}_{opt}^{Tx} .

From Fig. 4, we can also find that $R_{int}^{Tx}(\infty)$ cannot well approximate the high-frequency parts of $Z_{int}^{Tx}(f)$. Therefore, the energy spectral density could be different when evaluated using the Norton circuits in Figs. 1(c) and 5(a). Figs. 6(a) and (b) show the energy spectral density $E_{load}^{Tx}(f) = |I_{load}^{Tx}(f)|^2 Z_0$ for $Z_0 = 70 \Omega$ when $\tilde{P}_{opt}^{Tx} = 30$ mW and 160 mW, respectively. When \tilde{P}_{opt}^{Tx} is low [see Fig. 6(a)], the agreement is very good until 0.7 THz where most of the energy is contained. While at higher frequencies, the spectrum calculated from $R_{int}^{Tx}(\infty)$ is becoming different (2 dB at 2 THz). However, when \tilde{P}_{opt}^{Tx} increases and enters the saturation region, we can observe more significant difference between the spectra, as shown in Fig. 6(b). This is because $Z_{int}^{Tx}(f)$ varies more dramatically with high \tilde{P}_{opt}^{Tx} , as shown in Fig. 4(b). Therefore, we can use $R_{int}^{Tx}(\infty)$ to characterize the spectra in the relevant frequency band only before the power saturation.

III. NORTON EQUIVALENT CIRCUIT IN RECEPTION

In this section, we present the modeling of the current detected at a receiving PC gap via its corresponding Norton equivalent circuit. We consider the problem, as shown in Fig. 7(a), where a THz forward pulse wave $[v^+(t), i^+(t)]$ is propagating along an infinite transmission line. This wave can be, for instance, the one generated by the source geometry in Fig. 1(a). The transmission line is loaded with a PC gap excited by a pulsed laser. In this case, the derivation of the generator of the Norton circuit is standard by evaluating the transmission line when the load is short circuited, as shown in Fig. 7(b). At $z = 0$, the voltage amplitude of the forward wave and that of the reflected wave has the relation $v^+(t) = -v^-(t)$. Therefore, the generator current $i_{gen}^{Rx}(t)$ (with Rx superscript used to indicate the receiver) is the same as the total (short-circuited) current at $z = 0$, i.e., $i_{gen}^{Rx}(t) =$

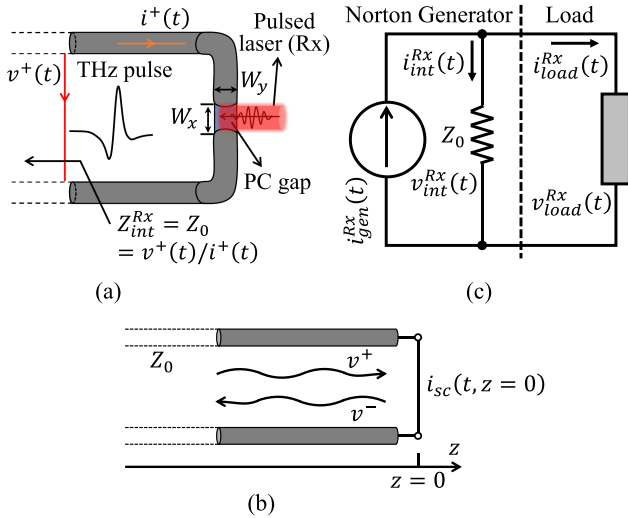


Fig. 7. (a) Schematic representation of a transmission line loaded with a PC gap. It is excited by a laser pulse, and at the same time, by a THz forward wave, $[v^+(t), i^+(t)]$, propagating along the transmission line. (b) Short-circuited transmission line model. $v^-(t)$ represents the reflected wave and $i_{sc}(t, z=0) = 2v^+(t)/Z_0$ is the total current at $z=0$. (c) Corresponding TD Norton equivalent circuit used to evaluate the time evolution of the THz voltage and current $[v_{load}^{Rx}(t), i_{load}^{Rx}(t)]$.

$i_{sc}(t, z=0)$, which is calculated as follows:

$$i_{gen}^{Rx}(t) = 2i^+(t) = 2v^+(t)/Z_0, \quad (6)$$

and the generator load is the impedance of the transmission line, i.e., Z_0 .

The laser pulses in Rx illuminate the PC gap periodically and free the electrons inside the gap. If the incoming THz wave is synchronized in time with a laser pulse, this wave will induce a time-varying current flowing across the gap. Such a process can be modeled in a Norton equivalent circuit by a load that has a time-varying constitutive relation related to the pulsed illumination on the PC gap. Accordingly, the TD Norton equivalent circuit for the PC receiver is shown in Fig. 7(c), which is similar to that in [40]. The load current $i_{load}^{Rx}(t)$ is evaluated using the constitutive (Drude) relation of the PC material

$$i_{load}^{Rx}(t) = \frac{q_e^2}{m_e} \frac{W_y W_z}{W_x} \int_{t_1}^t n_p^{Rx}(t, t') \int_{t''}^t e^{-\frac{t-t'}{\tau_s^{Rx}}} v_{load}^{Rx}(t') dt' dt'' \quad (7)$$

where t_1 is the time when the laser pulse arrives, and t is the current time. $n_p^{Rx}(t, t')$ has the same expression as (2) but with η_{gen}^{Rx} and \tilde{P}_{opt}^{Rx} as the generation efficiency and the optical power, respectively. The current and voltage in the generator load branch are indicated as $i_{int}^{Rx}(t)$ and $v_{int}^{Rx}(t) = v_{load}^{Rx}(t)$, respectively. The constitutive relation in this branch is given by the transmission line as $i_{int}^{Rx}(t) = v_{int}^{Rx}(t)/Z_0$.

The load current $i_{load}^{Rx}(t)$ exists only when the periodic THz waves are synchronized with the laser pulses in Rx. Fig. 8 illustrates such synchronization for different time-delayed laser pulses. Let us first focus on the left column of the figure: a

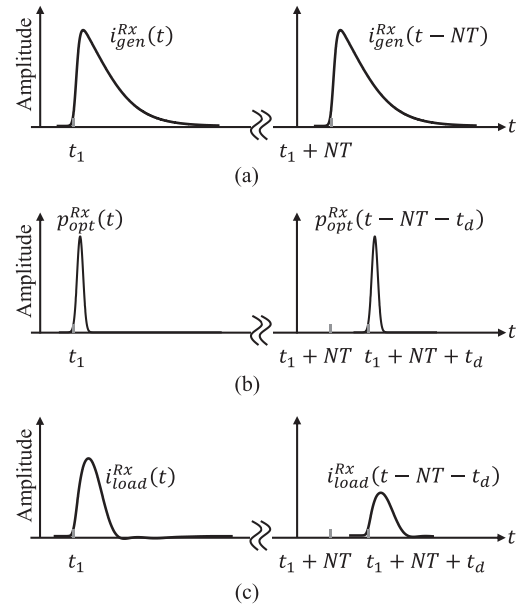


Fig. 8. Time evolution of the pulses in the Rx circuit for two periods. (a) Generator currents $i_{gen}^{Rx}(t)$. (b) Optical power pulses $p_{opt}^{Rx}(t)$. (c) Currents in the PC gap $i_{load}^{Rx}(t)$.

THz wave induces $i_{gen}^{Rx}(t)$ at time t_1 , as shown in Fig. 8(a). Let us then assume that the laser pulse $p_{opt}^{Rx}(t)$ is synchronized to arrive at the PC gap at also t_1 , as depicted in Fig. 8(b). Since the amplitude of $i_{gen}^{Rx}(t)$ reaches its maximum at the laser arrival, we obtain $i_{load}^{Rx}(t)$ with also high amplitude after t_1 , as shown in Fig. 8(c). Then, we examine the right column of Fig. 8 when several repetition time has passed and the time is at $t_1 + NT$ ($N = 1, 2, \dots$). The periodic THz wave induces $i_{gen}^{Rx}(t - NT)$, as shown in Fig. 8(a). At the same time, we add additional time delay t_d to the laser pulse to synchronize it with $i_{gen}^{Rx}(t - NT)$ at different times $t_1 + NT + t_d$ [see Fig. 8(b)]. The amplitude of $i_{gen}^{Rx}(t - NT)$ already starts to drop when the laser arrives; therefore, a lower $i_{load}^{Rx}(t - NT - t_d)$ is obtained [see Fig. 8(c)]. Of course, if the laser pulse is synchronized with the tail of $i_{gen}^{Rx}(t)$, $i_{load}^{Rx}(t)$ will be close to zero.

A. Marching-on-Time Solution of the Norton Circuit in Rx

Let us then solve the proposed TD Norton circuit for a specific period from the laser repetition time and a specific time delay for the laser pulse t_d . We impose the continuity of the currents at the node in the Rx Norton circuit in Fig. 7(c) as follows:

$$i_{gen}^{Rx}(t) = i_{int}^{Rx}(t, t_d) + i_{load}^{Rx}(t, t_d). \quad (8)$$

Before the laser arrival, i.e., $t \leq t_1$, we have the initial conditions that $i_{load}^{Rx}(t_1, t_d) = 0$ and $v_{load}^{Rx}(t_1, t_d) = 0$. We then use the current continuity to calculate the voltage at the following time $t_2 = t_1 + dt$, as follows:

$$v_{load}^{Rx}(t_2, t_d) = [i_{gen}^{Rx}(t_2) - i_{load}^{Rx}(t_1, t_d)] Z_0. \quad (9)$$

where dt is an infinitesimal time step. By substituting (9) into (7), we can obtain $i_{load}^{Rx}(t_2, t_d)$, and then we use the marching-on-time

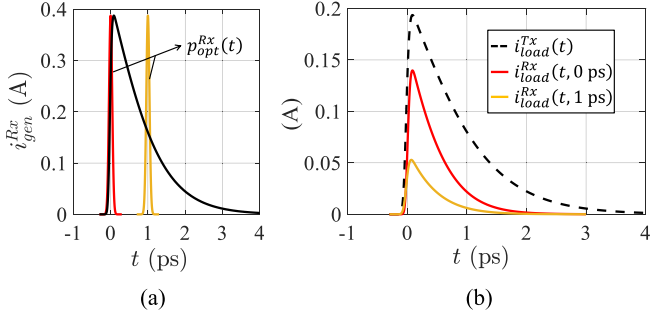


Fig. 9. (a) Generator current in Rx $i_{\text{gen}}^{\text{Rx}}(t)$ synchronized with the laser pulses in Rx with different time delays $t_d = 0$ ps and 1 ps. (b) Load currents in Rx $i_{\text{load}}^{\text{Rx}}(t, t_d)$ for different t_d and compared with the load current in Tx, $i_{\text{load}}^{\text{Tx}}(t)$. $\tau_c^{\text{Tx}} = \tau_c^{\text{Rx}} = 700$ fs, $\tau_s^{\text{Tx}} = \tau_s^{\text{Rx}} = 8.5$ fs, $\eta_{\text{gen}}^{\text{Tx}} = 25.6\%$, $\eta_{\text{gen}}^{\text{Rx}} = 16.6\%$, $\tilde{P}_{\text{opt}}^{\text{Tx}} = \tilde{P}_{\text{opt}}^{\text{Rx}} = 30$ mW, and $V_b = 30$ V.

technique to progressively solve the complete $i_{\text{load}}^{\text{Rx}}(t, t_d)$ and $v_{\text{load}}^{\text{Rx}}(t, t_d)$.

An example is shown here to highlight the currents in the proposed Rx circuit. Let us consider a case where the THz forward wave is the one generated in Fig. 2(b) when $\tilde{P}_{\text{opt}}^{\text{Tx}} = 30$ mW, i.e., $i_{\text{load}}^{\text{Tx}}(t)$. Fig. 9(a) shows the generator current $i_{\text{gen}}^{\text{Rx}}(t)$, which is the same as $i_{\text{load}}^{\text{Tx}}(t)$ but with the factor of 2 from (6), i.e., $i_{\text{gen}}^{\text{Rx}}(t) = 2i^+(t) = 2i_{\text{load}}^{\text{Tx}}(t)$. The PC gap and the laser source in Rx are the same as those in Tx. But the generation efficiencies are different: $\eta_{\text{gen}}^{\text{Tx}} = 25.6\%$, whereas $\eta_{\text{gen}}^{\text{Rx}} = 16.6\%$. These values are in line with the measurements, which will be explained in detail in Section V. We consider two cases of the laser delay in Rx, i.e., $t_d = 0$ ps and 1 ps, and the synchronization is shown in Fig. 9(a) with the laser amplitude normalized to $i_{\text{gen}}^{\text{Rx}}(t)$. Fig. 9(b) shows the solution of the marching-on-time evaluation for $i_{\text{load}}^{\text{Rx}}(t, t_d)$ with the corresponding time delay. It is compared with $i_{\text{load}}^{\text{Tx}}(t)$ and we can notice $i_{\text{load}}^{\text{Rx}}(t, 1 \text{ ps}) < i_{\text{load}}^{\text{Rx}}(t, 0 \text{ ps}) < i_{\text{load}}^{\text{Tx}}(t)$. This is because the impedance of the PC gap in Rx is also inversely proportional to $\tilde{P}_{\text{opt}}^{\text{Rx}}$, similarly to the case in Tx, as shown in Fig. 5(b). For our specific case, the load impedance is mismatched with the generator impedance (70 Ω).

B. Detected Currents in the PC Gap

For a specific time delay t_d , the load current $i_{\text{load}}^{\text{Rx}}(t, t_d)$ lasts in the order of ps, as shown in Fig. 9(b), so it cannot be easily detected instantaneously. Only the net charges $Q(t_d)$ associated with each pulse period can be measured. Accordingly, one can define the detected current $i_d(t_d)$ as the average of $Q(t_d)$ over the laser repetition time as follows:

$$i_d(t_d) = \frac{Q(t_d)}{T} = \frac{1}{T} \int_{t_1+t_d}^{t_1+t_d+T} i_{\text{load}}^{\text{Rx}}(t, t_d) dt. \quad (10)$$

Note that for each t_d , we only obtain a single dc value. If we sweep t_d and define a series of time delay as t_d ($\Delta t = 0, \Delta t, \dots, N\Delta t$ for $N + 1$ laser repetition time, with Δt the resolution of the time delay, then for each repetition, the laser pulse synchronizes with a different section of $i_{\text{gen}}^{\text{Rx}}(t)$. We assume that Δt is small enough and N is large enough so that the complete $i_{\text{gen}}^{\text{Rx}}(t)$ can be swept by the laser pulses. Typical values

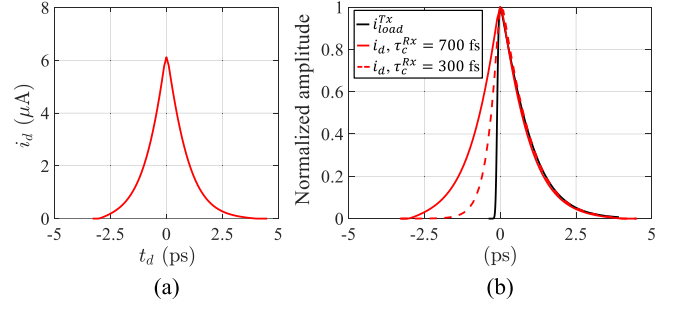


Fig. 10. Detected current $i_d(t_d)$. (a) Amplitude. (b) Waveform. $i_d(t_d)$ is compared with the load current in Tx $i_{\text{load}}^{\text{Tx}}(t)$. For the source, $\tau_c^{\text{Tx}} = 700$ fs, $\tau_s^{\text{Tx}} = 8.5$ fs, and $\eta_{\text{gen}}^{\text{Tx}} = 25.6\%$; while for the receiver, $\tau_c^{\text{Rx}} = 700$ fs and 300 fs are considered. $\tau_s^{\text{Rx}} = 8.5$ fs and $\eta_{\text{gen}}^{\text{Rx}} = 16.6\%$. $\tilde{P}_{\text{opt}}^{\text{Tx}} = \tilde{P}_{\text{opt}}^{\text{Rx}} = 30$ mW and $V_b = 30$ V.

for Δt are in the order of 0.1 ps. We, thus, can obtain a curve for the detected current for different time delays, i.e., $i_d(t_d)$, which is almost continuous.

An example of $i_d(t_d)$ is shown in Fig. 10, where its amplitude is plotted in Fig. 10(a) and its waveform is shown in Fig. 10(b) compared with that of $i_{\text{load}}^{\text{Tx}}(t)$. Thanks to the use of the Norton circuit, the actual amplitude of $i_d(t_d)$ can be evaluated. Moreover, we can notice that $i_d(t_d)$ is almost symmetric with respect to $t_d = 0$ ps and the waveform of $i_d(t_d \geq 0)$ is very close to that of $i_{\text{load}}^{\text{Tx}}(t \geq 0)$. The pulsewidth of $i_d(t_d)$ is doubled compared with $i_{\text{load}}^{\text{Tx}}(t)$ because of the long τ_c^{Rx} in Rx. During the recombination process in Rx, once a THz wave arrives at the PC gap in Rx, the remaining free electrons flow across the PC gap and form a time-varying current $i_{\text{load}}^{\text{Rx}}(t, t_d)$. Therefore, even when the laser is synchronized with $i_{\text{gen}}^{\text{Rx}}(t)$, for instance, at $t_d = -2.5$ ps, there is still a certain value of $i_d(t_d)$ and, thus, the complete $i_d(t_d)$ shows a symmetric behavior. According to this explanation, the shorter τ_c^{Rx} is, the better reconstruction can be achieved. If we use $\tau_c^{\text{Rx}} = 300$ fs while keeping other parameters the same, $i_d(t_d)$ is shown in Fig. 10(b) by the dashed curve. Apparently, in this case, $i_d(t_d)$ is much closer to $i_{\text{load}}^{\text{Tx}}(t)$. Ideally, if $\tau_c^{\text{Rx}} \rightarrow 0$, $i_{\text{load}}^{\text{Tx}}(t)$ can be completely reconstructed without distortion.

C. Fidelity Factor

We have seen that even if we have considered a nondispersive ideal link based on a transmission line, the detected current $i_d(t_d)$ is still distorted when compared with $i_{\text{load}}^{\text{Tx}}(t)$ due to the use of the long τ_c^{Rx} . If we further consider the use of antennas and QO components, the distortion could be worse. To quantify the pulse distortion from the Tx side to the Rx side, we evaluate the fidelity factor, which is typically used for ultrawideband antennas [41], [42]. It quantifies the distortion of a current $i_1(t)$ compared with a reference current $i_{\text{ref}}(t)$, and is expressed as follows:

$$F(i_1, i_{\text{ref}}) = \max_{\tau} \frac{\int_{-\infty}^{+\infty} i_{\text{ref}}(t) i_1(t - \tau) dt}{\sqrt{\int_{-\infty}^{+\infty} |i_{\text{ref}}(t)|^2 dt \int_{-\infty}^{+\infty} |i_1(t)|^2 dt}} \quad (11)$$

where τ is a certain time delay.

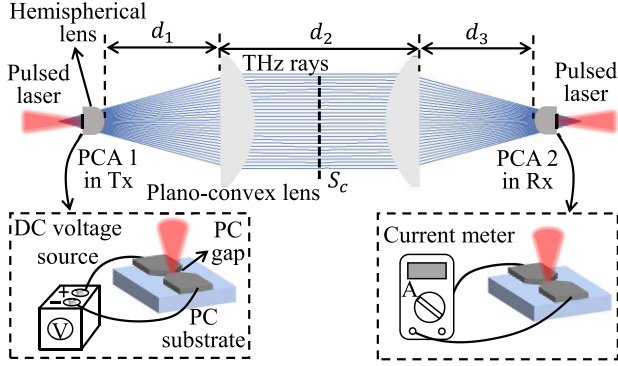


Fig. 11. Schematic representation of the QO link between two PCAs. The insets show the PCAs at the Tx and the Rx sides. The ray tracing of the field propagation along the link is shown by the blue rays.

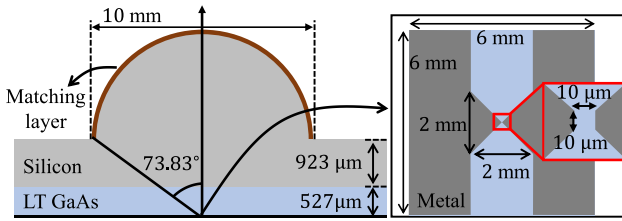


Fig. 12. BTA integrated with an extended hemispherical lens. The inset shows the detailed geometry of the BTA.

Let us first consider the fidelity factor in Tx between the load current $i_{\text{load}}^{\text{Tx}}(t)$ and the generator's current $i_{\text{gen}}^{\text{Tx}}(t)$, i.e., $F(i_{\text{load}}^{\text{Tx}}, i_{\text{gen}}^{\text{Tx}})$. We use the case, as shown in Fig. 2, and the fidelity factor is $F(i_{\text{load}}^{\text{Tx}}, i_{\text{gen}}^{\text{Tx}}) = 99\%$ and 93.3% for $\tilde{P}_{\text{opt}}^{\text{Tx}} = 30$ mW and 160 mW, respectively. This means as long as $\tilde{P}_{\text{opt}}^{\text{Tx}}$ is not in the saturation region, $i_{\text{load}}^{\text{Tx}}(t)$ should have very similar waveform as $i_{\text{gen}}^{\text{Tx}}(t)$. Then, for a nondispersive link, $F(i_{\text{gen}}^{\text{Rx}}, i_{\text{load}}^{\text{Tx}}) = 100\%$ according to (6). Finally, the fidelity factor between the detected current $i_d(t_d)$ and the load current in Tx $i_{\text{load}}^{\text{Tx}}(t)$ is calculated. For the case in Fig. 10(b), $F(i_d, i_{\text{load}}^{\text{Tx}}) = 90\%$ and 96.1% for $\tau_c^{\text{Rx}} = 700$ fs and 300 fs, respectively.

IV. QO LINK BETWEEN TWO PCAs

In this section, we model a more common scenario where two PCAs are integrated into lens antennas and coupled to each other via two free-standing plano-convex lenses, as shown in Fig. 11. Here, we consider the bow-tie-based PCAs fabricated in previous work [43]. As shown in Fig. 12, the bow-tie antenna (BTA) is processed on a substrate made of intrinsic LT GaAs and integrated with a silicon ($\epsilon_r = 11.9$) extended hemispherical lens. This lens has a diameter of 10 mm and an extension of 1.45 mm, and its phase center is 16 mm below the lens. Moreover, it is coated with a quarter-wavelength matching layer, which is made of parylene ($\epsilon_r = 2.72$) at 400 GHz. The inset shows the detailed bow-tie geometry, which has the width and length of 2 mm \times 2 mm, the gap size of 10 μm \times 10 μm , and the taper angle of 45° .

A. Norton Current Generator in Reception

This BTA presents almost constant and real input impedance below 1 THz, which can be approximated as a resistance, i.e., $Z_a(f) \approx R_a = 70 \Omega$, as discussed in [33]. Therefore, we can use the similar Norton equivalent circuits in Tx and Rx, as explained in the previous sections, where the load in Fig. 1(c) is $Z_0 = R_a \approx 70 \Omega$, and the generator impedance in Fig. 7(c) is also R_a . It is worth mentioning that the main limitation of these assumption is that we would not properly model the low frequencies where the PCAs become small in terms of wavelengths and stop working as broadband antennas (i.e., their input impedance will change significantly).

The QO link in Fig. 11 is similar to the scenarios, as shown in Figs. 1(a) and 7(a). However, now, the transmitted THz wave will suffer from dispersion due to the propagation through the link, in contrast to the nondispersive transmission line assumption taken previously. In terms of the modeling, the main difference is that the current generator of the Norton circuit in Rx will not be two times the load current in Tx as in (6). To evaluate this current generator in the presence of the QO link, we resort to the antenna in Rx formulism and the reciprocity theorem in FD [35], [36], which is very similar to the analysis in [11], [40], and [44]. There, the Thévenin open-circuit voltage $V_{\text{oc}}^{\text{Rx}}(f)$ was expressed as a field correlation on a decided surface S_c for each frequency

$$V_{\text{oc}}^{\text{Rx}}(f) I_0(f) = \frac{2}{\zeta_0} \int_{S_c} \vec{E}_{\text{PO-Tx}}^{S_c}(\vec{r}, f) \cdot \vec{E}_{\text{PO-Rx}}^{S_c}(\vec{r}, f) d\vec{r}, \quad (12)$$

where ζ_0 is the free-space impedance, $\vec{E}_{\text{PO-Tx}}^{S_c}(\vec{r}, f)$ is the spectral field amplitude radiated by the PCA in Tx from Fig. 11 on the surface S_c , $\vec{E}_{\text{PO-Rx}}^{S_c}(\vec{r}, f)$ is the field radiated by the PCA in Rx from Fig. 11 on S_c when it is operated in the Tx mode, and $I_0(f)$ is the current input at the receiving antenna when used in the Tx mode. Once the spectral Thévenin voltage $V_{\text{oc}}^{\text{Rx}}(f)$ is calculated, we can derive the corresponding spectral Norton current simply as $I_{\text{gen}}^{\text{Rx}}(f) = V_{\text{oc}}^{\text{Rx}}(f)/R_a$ and then derive its TD representation as follows:

$$i_{\text{gen}}^{\text{Rx}}(t) = \text{Re} \left[2 \int_0^\infty I_{\text{gen}}^{\text{Rx}}(f) e^{j2\pi ft} df \right]. \quad (13)$$

Here, one-sided inverse FT (IFT) is implemented since we only consider positive frequencies. The Norton circuit in Rx is then solved using the marching-on-time technique in (9).

B. Numerical Simulations of the QO Link

In order to evaluate (12), we use simulations done in two commercial software: CST [45] to obtain the PCA fields radiated into a semi-infinite silicon medium, and the PO solver of TICRA GRASP [46] to perform the field propagation from the silicon lens to the surface S_c . For convenience, S_c is taken in the middle of the link, as shown in Fig. 11. The fields radiated by both PCAs, $\vec{E}_{\text{PO-Tx}}^{S_c}(\vec{r}, f)$ and $\vec{E}_{\text{PO-Rx}}^{S_c}(\vec{r}, f)$, are the same at this plane because of the link symmetry; thus, only one needs to be numerically evaluated.

In CST, the BTA is excited with an impressed current in the gap with the amplitude of $I_{\text{CST}}(f)$. The far-field performance

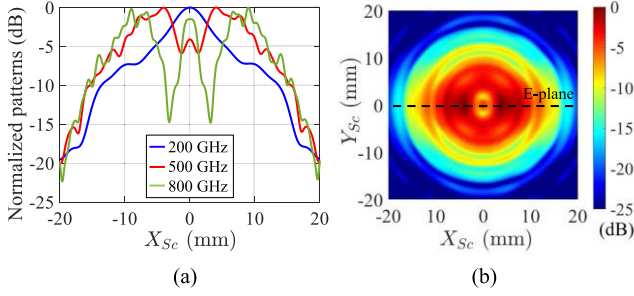


Fig. 13. Co-pol PO fields propagated to S_c evaluated using GRASP, $\vec{E}_{\text{PO-Tx}}^{S_c, \text{GRASP}}(f)$, in the (a) E -plane at 200, 500, and 800 GHz, and in the (b) XY -plane at 500 GHz.

of this BTA, when radiating inside the semi-infinite silicon medium, was discussed in [47]. The patterns at all frequencies oscillate significantly and their maxima are not at broadside. Therefore, they cannot illuminate the lens efficiently as explained in [34]. By using an in-house PO tool [36], the secondary fields radiated by the silicon lens in free space are evaluated. These fields were also discussed in [47] and they show nonbroadside and oscillating behaviors, especially at high frequencies. Although the used BTAs have poor radiation performance, they are available in our laboratory and we use them to validate the proposed model. To achieve better radiation performance, one can use the leaky lens antenna introduced in [34] and characterized in [47]. As discussed in these works, this type of antenna has a much higher gain than the BTA and couples better with the QO components.

The secondary fields are then propagated toward the left-side plano-convex lens, as shown in Fig. 11, and collimated by it. This lens (TPX 50) has a diameter of 35.5 mm, an effective focal length (EFL) of 50 mm, a thickness of 8.5 mm, and a refractive index of 1.46. The focus of this TPX lens is aligned with the phase center of the hemispherical lens. This setup was simulated in GRASP with the distance $d_1 = d_3 = 22.5$ mm and $d_2 = 150$ mm, and the ray tracing is shown by the blue rays. The simulated PO fields are defined as $\vec{E}_{\text{PO-Tx}}^{S_c, \text{GRASP}}(\vec{r}, f)$ and $\vec{E}_{\text{PO-Rx}}^{S_c, \text{GRASP}}(\vec{r}, f)$, which are identical in our case. The amplitude pattern of $\vec{E}_{\text{PO-Tx}}^{S_c, \text{GRASP}}(\vec{r}, f)$ is shown in Fig. 13(a) in the E -plane and, in Fig. 13(b), in the XY -plane (at 500 GHz). Here, the cartesian coordinate system with X_{S_c} and Y_{S_c} is used to represent the plane S_c . We also observe significant oscillation of the PO fields.

The PO field $\vec{E}_{\text{PO-Tx}}^{S_c, \text{GRASP}}(\vec{r}, f)$ is proportional to the CST impressed current $I_{\text{CST}}(f)$. Therefore, this field can be related to the PO field in (12), i.e., $\vec{E}_{\text{PO-Tx}}^{S_c}(\vec{r}, f)$, via the amplitude renormalization between $I_{\text{CST}}(f)$ and the load current in Tx, $I_{\text{load}}^{\text{Tx}}(f)$, as follows:

$$\vec{E}_{\text{PO-Tx}}^{S_c}(f) = \frac{I_{\text{load}}^{\text{Tx}}(f)}{I_{\text{CST}}(f)} \vec{E}_{\text{PO-Tx}}^{S_c, \text{GRASP}}(f). \quad (14)$$

If we substitute (14) into (12), the generator current $I_{\text{gen}}^{\text{Rx}}(f)$ can be calculated numerically. Using the normalization described in (14), the amplitude of $I_{\text{gen}}^{\text{Rx}}(f)$ is well modeled without introducing approximations as in [11].

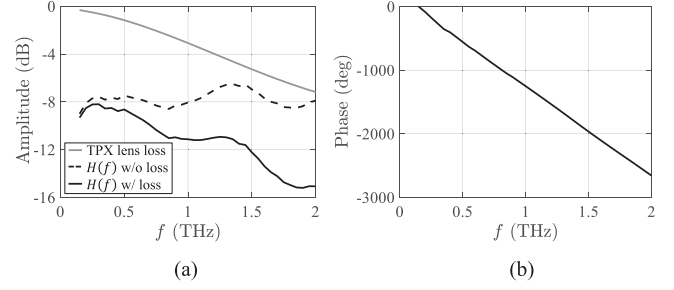


Fig. 14. Simulated link transfer function $H(f)$. (a) Amplitude. (b) Phase. The total dielectric loss of the used two TPX lenses is also shown.

Before we evaluate the current detected in the PC receiver, we can analyze the amplitude and phase dispersion of the QO link itself by means of the link transfer function $H(f)$. It only quantifies the field propagation between two PCAs and does not include the circuit analysis of the PC gaps. This means that $H(f)$ is independent of the Norton circuits discussed before and it is calculated as follows:

$$H(f) = \frac{\int_{S_c} \vec{E}_{\text{PO-Tx}}^{S_c, \text{GRASP}}(\vec{r}, f) \cdot \vec{E}_{\text{PO-Rx}}^{S_c, \text{GRASP}}(\vec{r}, f) d\vec{r}}{2\zeta_0 P_{\text{acc}}^{\text{CST}}(f)} \quad (15)$$

where $P_{\text{acc}}^{\text{CST}}(f) = 1/2 |I_{\text{CST}}(f)|^2 R_a$ is the accepted power in the CST simulations. $H(f)$ is always smaller than one and is independent of the actual current amplitude in the PC gaps. For the analyzed QO link and BTAs, the resulting amplitude of $H(f)$ is shown in Fig. 14(a). The total dielectric loss of the used two TPX lenses is also shown. Note that, for the mentioned PCA lens diameter (10 mm), the PO approach is not accurate when the frequency is below 150 GHz since the lens is too small. Therefore, the simulated $H(f)$ cannot be accurately estimated at low frequencies and we truncate it for $f < 150$ GHz (the proposed link is too large to simulate in a full-wave simulator below 150 GHz). This truncation will be performed for all frequency-related figures in the following. Due to the high dielectric loss and the poor radiation of the BTA mentioned before, the amplitude of $H(f)$ is quite low. The peaks in $H(f)$ are caused by the matching layer, which is resonant around 400 GHz and multiple frequencies. The phase of $H(f)$ is shown in Fig. 14(b). It presents linear behavior that corresponds to the forward-wave propagation along the QO link. Since $H(f)$ represents the dispersion of the QO link, by considering the field normalization in (14), the generator current in Rx, $I_{\text{gen}}^{\text{Rx}}(f)$, can be related to the load current in Tx, $I_{\text{load}}^{\text{Tx}}(f)$, via $H(f)$ as follows:

$$I_{\text{gen}}^{\text{Rx}}(f) = 2I_{\text{load}}^{\text{Tx}}(f) H(f). \quad (16)$$

C. Currents Detected in the PC Receiver

Let us now evaluate the detected currents of the PC receiver, as shown in Fig. 11. Here, we consider a biasing voltage of $V_b = 30$ V for the PCA in Tx, and the laser optical power of $\tilde{P}_{\text{opt}}^{\text{Tx}} = \tilde{P}_{\text{opt}}^{\text{Rx}} = 30$ mW. The recombination time is $\tau_c^{\text{Tx}} = \tau_c^{\text{Rx}} = 700$ fs, the scattering time is $\tau_s^{\text{Tx}} = \tau_s^{\text{Rx}} = 8.5$ fs, and the generation efficiency is $\eta_{\text{gen}}^{\text{Tx}} = 25.6\%$ and $\eta_{\text{gen}}^{\text{Rx}} = 16.6\%$.

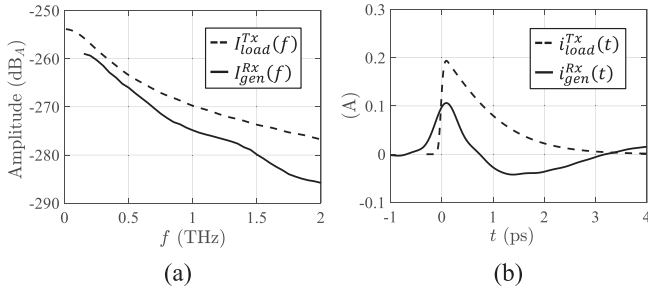


Fig. 15. Comparison between the generator current in Rx $I_{\text{gen}}^{\text{Rx}}(f)$ and the load current in Tx $I_{\text{load}}^{\text{Tx}}(f)$ in the (a) FD and (b) TD.

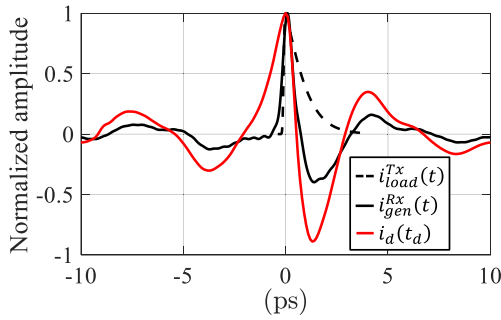


Fig. 16. Detected current $i_d(t_d)$ compared with the generator current in Rx $i_{\text{gen}}^{\text{Rx}}(t)$ and the load current in Tx $i_{\text{load}}^{\text{Tx}}(t)$ when the QO link in Fig. 11 is used. $\tau_c^{\text{Tx}} = \tau_c^{\text{Rx}} = 700$ fs, $\tau_s^{\text{Tx}} = \tau_s^{\text{Rx}} = 8.5$ fs, $\eta_{\text{gen}}^{\text{Tx}} = 25.6\%$, $\eta_{\text{gen}}^{\text{Rx}} = 16.6\%$, $\bar{P}_{\text{opt}}^{\text{Tx}} = \bar{P}_{\text{opt}}^{\text{Rx}} = 30$ mW, and $V_b = 30$ V.

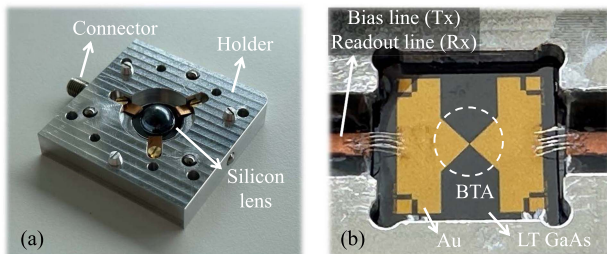


Fig. 17. Photographs of the measured bow-tie-based PCA. (a) Perspective view. (b) Bottom view.

By implementing the current relation in (16), the generator current in Rx, $I_{\text{gen}}^{\text{Rx}}(f)$, is calculated. It is shown in Fig. 15(a) and compared with the load current in Tx, $I_{\text{load}}^{\text{Tx}}(f)$. Here, $I_{\text{gen}}^{\text{Rx}}(f)$ is truncated for $f < 150$ GHz, as mentioned before, while $I_{\text{load}}^{\text{Tx}}(f)$ is not truncated since it corresponds to the $i_{\text{load}}^{\text{Tx}}(t)$ in Fig. 2(b). Due to the link propagation, $I_{\text{gen}}^{\text{Rx}}(f)$ is distorted and its amplitude follows the relation in (16). We then perform IFT on the spectral currents to obtain their time evolutions, which are shown in Fig. 15(b). The waveform of $i_{\text{gen}}^{\text{Rx}}(t)$ is also distorted and the amplitude drops in line with the spectral difference. Note that, besides the link propagation, the truncation of the spectral current also introduces distortion.

Finally, the detected current $i_d(t_d)$ is estimated using (10) and it is shown in Fig. 16 compared with $i_{\text{gen}}^{\text{Rx}}(t)$ and $i_{\text{load}}^{\text{Tx}}(t)$. Due to the use of the BTAs and the dispersive QO link, the THz pulse

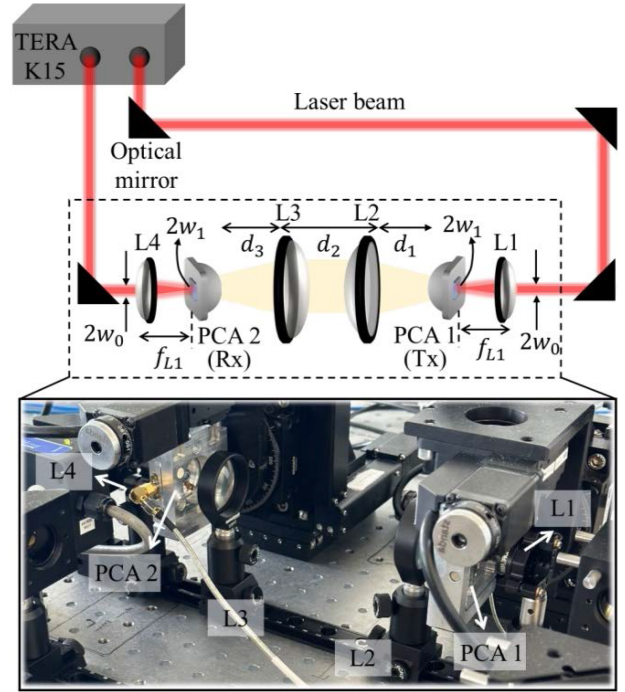


Fig. 18. Schematic representation of the measurement setup with the photograph shown in the inset. The laser beams are represented by the red rays, while the THz signals are the yellow rays. The indicated distance is $f_{L1} \approx 20.1$ mm, $d_1 = d_3 \approx 22.5$ mm, and $d_2 \approx 150$ mm.

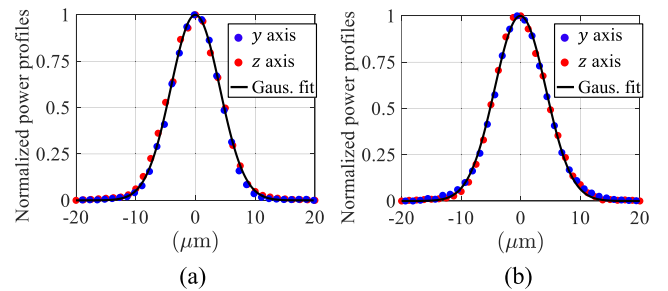


Fig. 19. Measured power profiles of the focused laser beams at the gaps of the PCAs in (a) Tx and (b) Rx. The black curves are the Gaussian fits of the measured points.

in Tx, i.e., $i_{\text{load}}^{\text{Tx}}(t)$, is distorted when arriving at the receiver. Such distortion (including the truncation distortion) is quantified by $F(i_{\text{gen}}^{\text{Rx}}, i_{\text{load}}^{\text{Tx}}) = 57.5\%$. Then, $i_{\text{gen}}^{\text{Rx}}(t)$ is reconstructed by $i_d(t_d)$. The waveform of $i_d(t_d)$ has wider pulsewidth and higher sidelobes compared with $i_{\text{gen}}^{\text{Rx}}(t)$ and the fidelity factor is $F(i_d, i_{\text{gen}}^{\text{Rx}}) = 90.8\%$. Such pulse distortion is mainly related to the very long recombination time of the receiver ($\tau_c^{\text{Rx}} = 700$ fs), which is similar to the case, as shown in Fig. 10(b). Finally, the total distortion of the link is calculated as $F(i_d, i_{\text{load}}^{\text{Tx}}) = 43.1\%$.

V. EXPERIMENTAL CHARACTERIZATION OF THE QO LINK AND THE RECEIVER

The proposed QO link, as shown in Fig. 11, with the above-mentioned bow-tie-based PCAs was measured in our laboratory at TU Delft. Fig. 17 shows a photograph of the measured PCA.

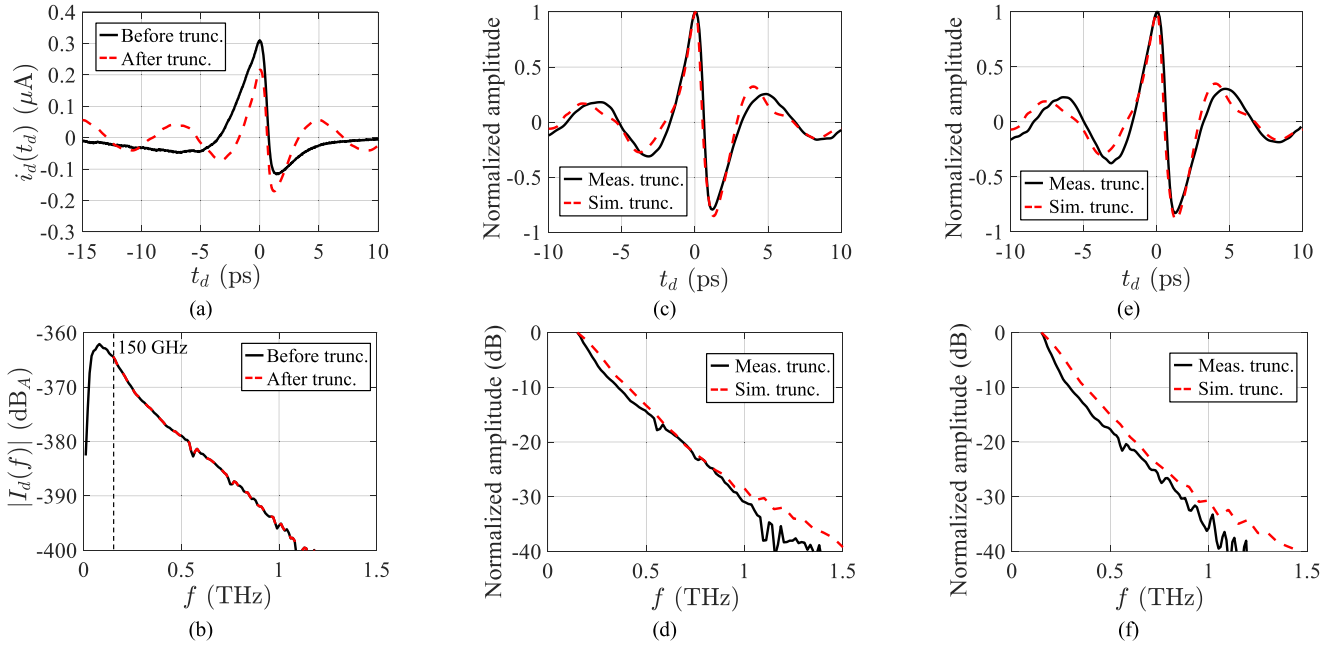


Fig. 20. Measured detected current of the PC receiver (PCA 2) when $V_b = 30$ V for the source (PCA 1) with $\tilde{P}_{\text{opt}}^{\text{Tx}} = 10$ mW and $\tilde{P}_{\text{opt}}^{\text{Rx}} = 9$ mW. (a) Time signal. (b) Spectrum. The spectrum truncated for $f < 150$ GHz is shown by the dashed curve in (b). Measured detected currents (after truncation) compared with the simulations. (c) and (d) correspond to $\tilde{P}_{\text{opt}}^{\text{Tx}} = 10$ mW and $\tilde{P}_{\text{opt}}^{\text{Rx}} = 9$ mW. (e) and (f) are $P_{\text{opt}}^{\text{Tx}} = 30$ mW and $\tilde{P}_{\text{opt}}^{\text{Rx}} = 28$ mW. The amplitude of the time signals is normalized to the maxima at $t_d = 0$. The spectra are normalized to $f = 150$ GHz and the loss of the TPX lenses in Fig. 14(a) is included in the simulations.

The PCA is mounted on a holder, as explained in [48]. The PCA holder has an SMA connector, which is used either to bias the PC source or to read out the current detected by the PC receiver. A schematic of the measurement setup, together with a photograph of it, is shown in Fig. 18. This setup uses the free-space 780 nm laser output of a commercial THz spectrometer TERA K15 from Menlo Systems [37] to optically illuminate our PCAs. We split the output laser power equally for both laser ports and the maximum output power is about 100 mW per port. The PC source is biased by a dc power supply with the voltage V_b , whereas the PC receiver is connected to a dc current meter.

The output laser beam arriving at L1 has a $1/e^2$ radius of $w_0 \approx 0.7$ mm. To achieve the ideal illumination on the gap of the PCA, we use a plano-convex lens L1 to focus the incoming laser beams (see Fig. 18). This lens is LA1074-B-ML from Thorlabs and has a diameter of 12.7 mm and an EFL of 20 mm. The focused laser beam has a radius of $w_1 = 8.5$ μm . This corresponds to the FWHM of 10 μm , which is the same as the gap size of the PCA, i.e., $\text{FWHM} = W_x = W_y$. Note that the free-space optical path for the source in Fig. 18 is longer than that of the receiver. This is because the optical path of the port in Tx is shorter than that in Rx inside TERA K15 and we need to add this extra length to assure that the detected THz signal is within the range of the optical delay unit (ODU) of TERA K15.

The spot sizes of the focused laser beams in both Tx and Rx were measured along two orthogonal axes (y and z axes) using the knife-edge technique with two metal blades [48]. The results are shown in Fig. 19(a) and (b) for the source (PCA 1) and the receiver (PCA 2), respectively. The amplitude of the power

profiles is normalized to the laser power after the focusing lens L1 and L4, which is $\tilde{P}_L^{\text{Tx}} \approx \tilde{P}_L^{\text{Rx}} \approx 94$ mW, respectively. Thanks to the extensive alignment procedures, the profiles have excellent Gaussian shapes for both laser ports. The FWHM of the source is 9.3 μm (y -axis) and 10 μm (z -axis), which leads to an average spillover efficiency on the PC gap of 60.5%. By also considering the absorption efficiency of the LT GaAs substrate, the optical efficiency is $\eta_{\text{opt}}^{\text{Tx}} = \tilde{P}_{\text{opt}}^{\text{Tx}} / \tilde{P}_L^{\text{Tx}} \approx 35.7\%$. While for the receiver, the FWHM is 10.1 μm for both axes; thus, the average spillover and optical efficiency is 57.1% and $\eta_{\text{opt}}^{\text{Rx}} = \tilde{P}_{\text{opt}}^{\text{Rx}} / \tilde{P}_L^{\text{Rx}} \approx 33\%$, respectively.

We then measure the currents detected at the receiver using the setup in Fig. 18, similar to what was done in [49] and [50]. To synchronize the receiver with the source, we fix the optical path of the laser pulses in Tx and change the one in Rx by using the ODU inside TERA K15. The measured $i_d(t_d)$ is shown in Fig. 20(a) when $V_b = 30$ V for the PC source with $\tilde{P}_{\text{opt}}^{\text{Tx}} = 10$ mW and $\tilde{P}_{\text{opt}}^{\text{Rx}} = 9$ mW, and its corresponding spectrum $I_d(f)$ is plotted in Fig. 20(b). The amplitude of $i_d(t_d)$ is measured using a Keithley 2000 multimeter with an integration time of 200 ms. We obtain a fidelity factor $F(i_d, i_{\text{load}}^{\text{Tx}}) = 65\%$ comparing the waveform of $i_d(t_d)$ with the load current in Tx $i_{\text{load}}^{\text{Tx}}(t)$. Since the PO approach is not accurate when the frequency is below 150 GHz, we need to truncate the measured spectrum for $f < 150$ GHz [see Fig. 20(b)] to have a fair comparison with our simulations. We then perform the IFT on the truncated spectrum to obtain the corresponding time signal, which is plotted in Fig. 20(a) by the dashed curve. This curve shows that the low-frequency spectrum has a strong impact on

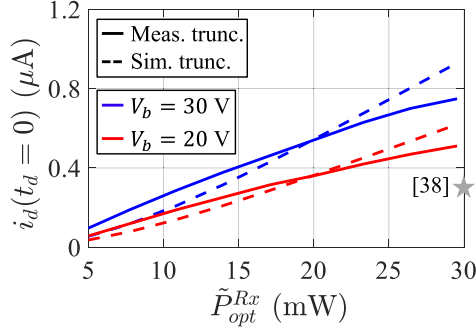


Fig. 21. Measured DC currents at the maxima position ($t_d = 0$) in Fig. 20 compared with the simulations. Two biasing voltages $V_b = 20$ V and 30 V are considered for the source. The current measured using the Menlo Systems [38] is also shown.

the detected current. After the truncation, the width of $i_d(t_d)$ significantly decreases with higher sidelobes and lower main lobe. The fidelity factor now becomes 46.5% (including the truncation distortion). This current and its truncated spectrum are referred to as the measured current and spectrum in the following for convenience.

Following the procedures, as discussed in Section III, we can solve the Rx circuit for different time delays and obtain the simulated detected current $i_d(t_d)$. To best fit the waveform of the measured pulse in Fig. 20(a), the recombination time of both PCAs is found to be the same, and their values are set as $\tau_c^{\text{Tx}} = \tau_c^{\text{Rx}} = 700$ fs. In Appendix B, we have shown that the PC source (PCA 1) radiates more power than the receiver (PCA 2) due to different material properties. To best match our simulations with the power measurements, the scattering time of both PCAs is set to be $\tau_s^{\text{Tx}} = \tau_s^{\text{Rx}} = 8.5$ fs, and the generation efficiency is $\eta_{\text{gen}}^{\text{Tx}} = 25.6\%$ and $\eta_{\text{gen}}^{\text{Rx}} = 16.6\%$.

Then, we substitute these parameters into the simulations compared with the measurements. The comparison is shown in Fig. 20(c) and (d) for $\tilde{P}_{\text{opt}}^{\text{Tx}} = 10$ mW and $\tilde{P}_{\text{opt}}^{\text{Rx}} = 9$ mW, and in Fig. 20(e) and (f) for $\tilde{P}_{\text{opt}}^{\text{Tx}} = 30$ mW and $\tilde{P}_{\text{opt}}^{\text{Rx}} = 28$ mW. The simulated spectra are also truncated for $f < 150$ GHz and the agreement with the measurements in both cases is excellent. These spectra decrease fast because τ_c of both PCAs is very long. By performing IFT, the simulated detected currents are also in excellent agreement with the measurements. Furthermore, we measured the maximum detected dc currents when the laser pulses in Rx are synchronized with the peaks of the THz pulses. This corresponds to the maxima position ($t_d = 0$) shown in Fig. 20(c) and (e). These dc currents are calculated when the spectra are truncated and are plotted in Fig. 21 versus $\tilde{P}_{\text{opt}}^{\text{Rx}}$. The simulations were done under the same conditions and they match well with the measurements for different V_b . Such good matching further confirms that $\tau_s^{\text{Tx}}/\tau_s^{\text{Rx}}$ and $\eta_{\text{gen}}^{\text{Tx}}/\eta_{\text{gen}}^{\text{Rx}}$ are properly evaluated. As a reference, when using the source and the receiver from Menlo Systems [38], the measured dc current is less than $0.4 \mu\text{A}$ when $\tilde{P}_{\text{opt}}^{\text{Rx}} \approx 30$ mW and $V_b = 100$ V. To our best knowledge, this is the first time that the detected currents are simulated in a link between PCAs and compared with the measurements in both the waveforms and the amplitude.

VI. CONCLUSION

In this work, we characterize the generation and detection of the THz pulses between a pulsed PC source and a receiver via the TD Norton equivalent circuits. We first briefly introduce the TD Norton circuit for the PC source. To simplify the numerical time-marching evaluation of the TD circuit, we introduce a constant generator resistance and propose an approximated FD circuit. This circuit can be solved analytically and is capable of accurately predicting the radiated power. Therefore, this circuit is a very powerful tool to analyze and design PC sources, especially when the goal is to maximize the radiated power, without spending more optical power than necessary.

We then consider a nondispersive transmission line as the QO link to analyze the PC receiver. A similar TD Norton equivalent circuit is proposed to characterize the photocurrents in the receiving PC gap. Afterward, a stroboscopic sampling process is implemented to evaluate the detected currents. It is found that the reconstruction quality (fidelity factor) of the detected currents with respect to the load currents in Tx is directly related to the recombination time of the receiver. Finally, we analyze a dispersive QO link between two bow-tie-based PCAs using a field correlation approach. The fields radiated by the PCAs are evaluated in the middle of the link using the full-wave simulations combined with a PO approach. These fields are used to calculate the link transfer function and the current generator of the receiving Norton circuit. The detected currents are then reconstructed in both amplitude and waveforms.

To validate our proposed modeling methodology, we measured the detected currents at the PC receiver using the proposed QO link. The measurements of the pulsewidth indicate that the used PCAs have a long recombination time of 700 fs. After truncating the measured spectra for $f < 150$ GHz, the corresponding time signals are in excellent agreement with the simulations. We also compare the peak amplitude of the detected dc currents, showing very good agreement. The proposed methodology is validated and is applicable to different PCA structures and QO links. Therefore, this method can be used to analyze and optimize the generation and detection of THz pulses for future imaging and spectroscopy applications.

APPENDIX A

APPROXIMATION OF THE NORTON EQUIVALENT CIRCUIT IN TRANSMISSION

To simplify the time-marching evaluation of the TD Norton equivalent circuit, we approximate the nonlinear constitutive relation of the internal generator current in (3) as a simple resistance, which was also discussed in [39]. To achieve this, we introduce an auxiliary quantity defined as the *pseudo energy* dissipated in the Norton generator load branch, which can be evaluated as follows:

$$E_{\text{pseudo}}^{\text{Tx}}(Z_0) = \int_{t_0}^{t_0+T} v_{\text{int}}^{\text{Tx}}(t, Z_0) i_{\text{int}}^{\text{Tx}}(t, Z_0) dt. \quad (\text{A.1})$$

Here, $E_{\text{pseudo}}^{\text{Tx}}$ is indicated as the *pseudoenergy* because it does not represent the actual energy dissipated in the gap and the proposed Norton circuit does not model the dc components [32].

It is convenient to introduce an equivalent generator resistance $R_{\text{int}}^{\text{Tx}}(Z_0)$ that is constant in time and would provide the same energy dissipation as in the internal generator branch in (A.1)

$$\begin{aligned} E_{\text{pseudo}}^{\text{Tx}}(Z_0) &= \int_{t_0}^{t_0+T} R_{\text{int}}^{\text{Tx}}(Z_0) [i_{\text{int}}^{\text{Tx}}(t, Z_0)]^2 dt \\ \Rightarrow R_{\text{int}}^{\text{Tx}}(Z_0) &= \frac{\int_{t_0}^{t_0+T} v_{\text{int}}^{\text{Tx}}(t, Z_0) i_{\text{int}}^{\text{Tx}}(t, Z_0) dt}{\int_{t_0}^{t_0+T} [i_{\text{int}}^{\text{Tx}}(t, Z_0)]^2 dt}. \end{aligned} \quad (\text{A.2})$$

Fig. 5(b) shows the values of $R_{\text{int}}^{\text{Tx}}(Z_0)$ calculated using the time-marching method versus the laser optical power $\tilde{P}_{\text{opt}}^{\text{Tx}}$ when different loads are considered, i.e., $Z_0 = 20 \Omega$, 70Ω , and 300Ω . The corresponding $R_{\text{int}}^{\text{Tx}}(Z_0)$ is comparable to $Z_{\text{int}}^{\text{Tx}}(f)$ in Fig. 4 at low frequencies. Moreover, the curves of $R_{\text{int}}^{\text{Tx}}(Z_0)$ for all Z_0 values are quite close to each other, so we can assume that $R_{\text{int}}^{\text{Tx}}(Z_0)$ is independent from the load resistance. It suggests that we can solve the circuit for $Z_0 = \infty$. In this case, the load plays no role and the voltage-to-current relation can be evaluated analytically without the marching-on-time procedures, using the approximations discussed in the following sections.

A. Very Short Carrier Scattering Time

When the carrier scattering time τ_s^{Tx} is very short (for LT GaAs, τ_s^{Tx} is in the order of 10 fs), the exponential term in (3), i.e., $e^{-(t-t')/\tau_s^{\text{Tx}}}$, decreases very rapidly with respect to the voltage evolution $v_{\text{int}}^{\text{Tx}}(t')$. In such a situation, we can assume that $v_{\text{int}}^{\text{Tx}}(t')$ is constant in the time interval where the exponential term is significantly different from zero so that the inner integral in (3) can be approximated as follows:

$$\begin{aligned} \int_{t''}^t e^{-\frac{t-t'}{\tau_s^{\text{Tx}}}} v_{\text{int}}^{\text{Tx}}(t') dt' &\cong v_{\text{int}}^{\text{Tx}}(t) \int_{t''}^t e^{-\frac{t-t'}{\tau_s^{\text{Tx}}}} dt' \\ &= v_{\text{int}}^{\text{Tx}}(t) \tau_s^{\text{Tx}} \left(1 - e^{-\frac{t-t''}{\tau_s^{\text{Tx}}}}\right). \end{aligned} \quad (\text{A.3})$$

Accordingly, the current $i_{\text{int}}^{\text{Tx}}(t)$ in (3) can be approximated as follows:

$$\begin{aligned} i_{\text{int}}^{\text{Tx}}(t) &\cong \frac{\tau_s^{\text{Tx}} q_e^2}{m_e} \frac{W_y W_z}{W_x} v_{\text{int}}^{\text{Tx}}(t) \\ &\int_{t_0}^t n_p^{\text{Tx}}(t, t'') \left(1 - e^{-\frac{t-t''}{\tau_s^{\text{Tx}}}}\right) dt''. \end{aligned} \quad (\text{A.4})$$

If we next consider LT GaAs as the photoconductor material, i.e., we assume $\tau_c^{\text{Tx}} \gg \tau_s^{\text{Tx}}$, (A.4) can be further approximated as follows:

$$\begin{aligned} i_{\text{int}}^{\text{Tx}}(t) &\cong \frac{\tau_s^{\text{Tx}} q_e^2}{m_e} \frac{T}{W_x^2} \frac{\eta_{\text{gen}}^{\text{Tx}} \tilde{P}_{\text{opt}}^{\text{Tx}}}{h f_c} v_{\text{int}}^{\text{Tx}}(t) \\ &\int_{t_0}^t \frac{1}{\tau_p} \sqrt{\frac{4 \ln 2}{\pi}} e^{-4 \ln 2 \left(\frac{t''}{\tau_p}\right)^2} \left(e^{-\frac{t-t''}{\tau_c^{\text{Tx}}}} - e^{-\frac{t-t''}{\tau_s^{\text{Tx}}}}\right) dt''. \end{aligned} \quad (\text{A.5})$$

Equation (A.5) is similar to the corresponding expression in [51], but here (A.5) retains the dependence of the current at time t that accounts for the history of the voltage on the gap.

B. Instantaneous Laser Pulses

The integral in (A.5) can be easily evaluated numerically; however, to acquire deeper physical understanding, we can further assume that the laser pulse duration is instantaneous, i.e., $\tau_p \rightarrow 0$. Under this hypothesis, the term $\frac{1}{\tau_p} \sqrt{\frac{4 \ln 2}{\pi}} e^{-4 \ln 2 \left(\frac{t''}{\tau_p}\right)^2}$ becomes a Dirac delta function $\delta(t'')$. Thus, for $t > 0$, $i_{\text{int}}^{\text{Tx}}(t)$ can be written as follows:

$$i_{\text{int}}^{\text{Tx}}(t) \cong \mu_{\text{dc}}^{\text{Tx}} \frac{q_e T}{W_x^2} \frac{\eta_{\text{gen}}^{\text{Tx}} \tilde{P}_{\text{opt}}^{\text{Tx}}}{h f_c} v_{\text{int}}^{\text{Tx}}(t) \left(e^{-\frac{t}{\tau_c^{\text{Tx}}}} - e^{-\frac{t}{\tau_s^{\text{Tx}}}}\right) \quad (\text{A.6})$$

where $\mu_{\text{dc}}^{\text{Tx}} = \tau_s^{\text{Tx}} q_e / m_e$ is the dc mobility of the PC material. It is worth noting that, in the time interval $t = (2\tau_s^{\text{Tx}}, \infty)$, $e^{-t/\tau_s^{\text{Tx}}}$ in (A.6) becomes negligible with respect to $e^{-t/\tau_c^{\text{Tx}}}$ since we assume $\tau_c^{\text{Tx}} \gg \tau_s^{\text{Tx}}$. Thus, the value of $i_{\text{int}}^{\text{Tx}}(t)$ is mainly related to the recombination rate of the excited electrons.

For the LT GaAs discussed in this article, the single integral approximation that leads to (A.5) is well justified, while the approximation resulting in (A.6) is rougher since the pulse duration could be comparable to the recombination time.

Nevertheless, (A.6) can be used to estimate the current $i_{\text{int}}^{\text{Tx}}(t, Z_0)$ in (A.2) to obtain $R_{\text{int}}^{\text{Tx}}(Z_0)$. Here, since $R_{\text{int}}^{\text{Tx}}(Z_0)$ is almost independent of the load [see Fig. 5(b)], we assume that $Z_0 = \infty$. This corresponds to an open-circuit case and, thus, the voltage on the gap is assumed to remain constant as equal to the biasing voltage V_b . By substituting $v_{\text{int}}^{\text{Tx}}(t) = v_{\text{load}}^{\text{Tx}}(t) = V_b$ into (A.6), we obtain an analytical expression for $i_{\text{int}}^{\text{Tx}}(t)$. Then, the Norton resistance in (A.2) can be analytically calculated and the expression is shown by (5).

APPENDIX B

MEASUREMENTS OF THE RADIATED THZ POWER

PCA 1 (the source) and PCA 2 (the receiver) have identical geometries; however, since they were fabricated from different locations on the same LT GaAs wafer, they could have different material properties. To quantify the recombination time, the scattering time, and the generation efficiency for the used PCAs, besides the current measurements, as described in Section V, we also measured the THz power radiated by each PCA using the setup, as shown in Fig. 22 (similar to what was done in [33]). We use a PM5 power meter (Virginia Diodes) connected to a conical WR10 horn antenna to capture the THz fields focused by the focusing lens L3.

The measured power is shown in Fig. 23 for a biasing voltage of $V_b = 30$ V versus the optical power $\tilde{P}_{\text{opt}}^{\text{Tx}}$ in the gap. We can observe that even if the used PCAs and the measurement setups are identical, different radiated powers are detected. From this, we can conclude that the used LT GaAs substrate of each PCA has different material properties. The recombination time of the PC material is mainly associated with the width of the radiated THz pulses, thus the integration time for the power. We estimate its value according to the measurements of the detected currents, as discussed in Section V, and $\tau_c^{\text{Tx}} = \tau_c^{\text{Rx}} = 700$ fs. In our model, the radiated power is also proportional to the values of the scattering time and the generation efficiency. Since PCA 1 radiates about 4 dB higher power than PCA 2, we can assume

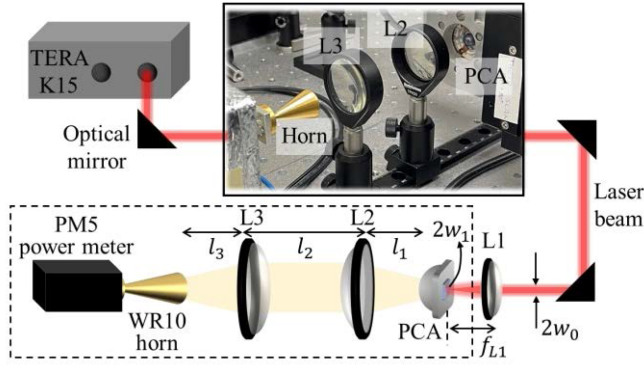


Fig. 22. Schematic representation of the setup for the power measurement with the photograph shown in the inset. The laser beams are represented by the red rays, while the THz signals are the yellow rays. The indicated distance is $f_{L1} \approx 20.1$ mm, $l_1 \approx 22.5$ mm, $l_2 \approx 63$ mm, and $l_3 \approx 20$ mm.

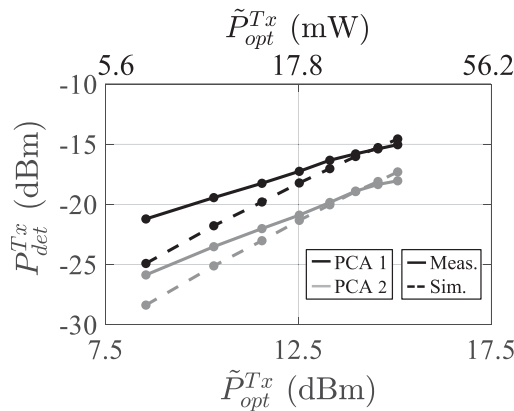


Fig. 23. Measurements and simulations of the radiated THz power P_{det}^{Tx} for both PCAs when using the setup in Fig. 22. PCA 1 is later used as the source, while PCA 2 is the receiver. In the simulations, $V_b = 30$ V, $\tau_c^{Tx} = \tau_c^{Rx} = 700$ fs, $\tau_s^{Tx} = \tau_s^{Rx} = 8.5$ fs, $\eta_{gen}^{Tx} = 25.6\%$, and $\eta_{gen}^{Rx} = 16.6\%$.

that $\tau_s^{Tx} \eta_{gen}^{Tx} \approx 1.6 \tau_s^{Rx} \eta_{gen}^{Rx}$. We then apply the same procedures described in [33] to obtain the EM simulations of the setup. Note that the accuracy of the simulations for the QO link is limited below 150 GHz, as explained in Section IV. We estimate the values of $\tau_s^{Tx} / \tau_s^{Rx}$ and $\eta_{gen}^{Tx} / \eta_{gen}^{Rx}$ for both PCAs by matching the power simulations with the measurements. Eventually, we set $\tau_s^{Tx} = \tau_s^{Rx} = 8.5$ fs (in line with the values in [33]), $\eta_{gen}^{Tx} = 25.6\%$, and $\eta_{gen}^{Rx} = 16.6\%$ (as the fitting parameters) for the best match, as shown in Fig. 23. η_{gen}^{Rx} has a lower value possibly because the LT GaAs is not properly annealed [43], [52], [53], [54], as the measured dark resistance of PCA 2 (50 M Ω) is much lower than that of PCA 1 (∞ Ω).

REFERENCES

- [1] D. H. Auston, K. P. Cheung, and P. R. Smith, "Picosecond photoconducting Hertzian dipoles," *Appl. Phys. Lett.*, vol. 45, no. 3, pp. 284–286, Aug. 1984.
- [2] D. Grischkowsky, S. Keiding, M. van Exter, and C. Fattinger, "Far-infrared time-domain spectroscopy with terahertz beams of dielectrics and semiconductors," *J. Opt. Soc. Amer. B*, vol. 7, no. 10, pp. 2006–2015, Oct. 1990.
- [3] P. U. Jepsen, D. G. Cooke, and M. Koch, "Terahertz spectroscopy and imaging—Modern techniques and applications," *Laser Photon. Rev.*, vol. 5, no. 1, pp. 124–166, Jan. 2011.
- [4] N. M. Burford and M. O. El-Shenawee, "Review of terahertz photoconductive antenna technology," *Opt. Eng.*, vol. 56, no. 1, Jul. 2017, Art. no. 010901.
- [5] H. Guerboukha, K. Nallappan, and M. Skorobogatiy, "Toward real-time terahertz imaging," *Adv. Opt. Photon.*, vol. 10, no. 4, pp. 843–938, Dec. 2018.
- [6] A. F. Bernardis, P. M. Sberna, A. Neto, and N. Llombart, "Signal to noise ratio budget of a pico-seconds pulsed radar system for stand-off imaging," in *Proc. 44th Int. Conf. Infrared, Millimeter, THz Waves*, 2019, pp. 1–2.
- [7] R. Henri et al., "Fabrication and characterization of an 8 \times 8 terahertz photoconductive antenna array for spatially resolved time domain spectroscopy and imaging applications," *IEEE Access*, vol. 9, pp. 117691–117702, Aug. 2021.
- [8] P. Benicewicz, J. Roberts, and A. Taylor, "Scaling of terahertz radiation from large-aperture biased photoconductors," *J. Opt. Soc. Amer. B*, vol. 11, no. 12, pp. 2533–2546, Dec. 1994.
- [9] P. U. Jepsen, R. H. Jacobsen, and S. R. Keiding, "Generation and detection of terahertz pulses from biased semiconductor antennas," *J. Opt. Soc. Amer. B*, vol. 13, no. 11, pp. 2424–2436, Nov. 1996.
- [10] M. Tani, S. Matsuura, K. Sakai, and S. Nakashima, "Emission characteristics of photoconductive antennas based on low-temperature-grown GaAs and semi-insulating GaAs," *Appl. Opt.*, vol. 36, no. 30, pp. 7853–7859, Oct. 1997.
- [11] S.-G. Park, M. R. Melloch, and A. M. Weiner, "Analysis of terahertz waveforms measured by photoconductive and electrooptic sampling," *IEEE J. Quantum Electron.*, vol. 35, no. 5, pp. 810–819, May 1999.
- [12] L. Duvillearet, F. Garet, J.-F. Roux, and J.-L. Coutaz, "Analytical modeling and optimization of terahertz time-domain spectroscopy experiments, using photoswitches as antennas," *IEEE J. Sel. Topics Quantum Electron.*, vol. 7, no. 4, pp. 615–623, Jul./Sep. 2001.
- [13] I. Kostakis, D. Saeedkia, and M. Missous, "Terahertz generation and detection using low temperature grown InGaAs-InAlAs photoconductive antennas at 1.55 μ m pulse excitation," *IEEE Trans. THz Sci. Technol.*, vol. 2, no. 6, pp. 617–622, Nov. 2012.
- [14] N. Khiabani, Y. Huang, Y.-C. Shen, S. Boyes, and Q. Xu, "A novel simulation method for THz photoconductive antenna characterization," in *Proc. Eur. Conf. Antennas Propag.*, 2013, pp. 751–754.
- [15] A. Jooshesh, "Plasmonic-enhanced THz generation and detection using photoconductive antennas," Ph.D. dissertation, Dept. Elect. Comput. Eng., Univ. of Victoria, Victoria, BC, Canada, 2016.
- [16] B. Petrov, A. Fekecs, C. Sarra-Bournet, R. Arès, and D. Morris, "Terahertz emitters and detectors made on high-resistivity InGaAsP:Fe photoconductors," *IEEE Trans. THz Sci. Technol.*, vol. 6, no. 5, pp. 747–753, Sep. 2016.
- [17] R. Smith, A. Jooshesh, J. Zhang, and T. Darcie, "Photoconductive generation and detection of THz-bandwidth pulses using near-field coupling to a free-space metallic slit waveguide," *Opt. Exp.*, vol. 25, no. 22, pp. 26492–26499, Oct. 2017.
- [18] T. K. Nguyen et al., "Photoconductive dipole antennas for efficient terahertz receiver," *Opt. Commun.*, vol. 383, pp. 50–56, Jan. 2017.
- [19] D. V. Lavrukhin et al., "Strain-induced InGaAs-based photoconductive terahertz antenna detector," *IEEE Trans. THz Sci. Technol.*, vol. 11, no. 4, pp. 417–424, Jul. 2021.
- [20] E. Moreno, M. F. Fernández Pantoja, S. G. Garcia, A. R. Bretones, and R. G. Gómez Martin, "Time-domain numerical modeling of THz photoconductive antennas," *IEEE Trans. THz Sci. Technol.*, vol. 4, no. 4, pp. 490–500, Jul. 2014.
- [21] N. Burford and M. El-Shenawee, "Computational modeling of plasmonic thin-film terahertz photoconductive antennas," *J. Opt. Soc. Amer. B*, vol. 33, no. 4, pp. 748–759, Apr. 2016.
- [22] G. C. Loata, M. D. Thomson, T. Lffler, and H. G. Roskos, "Radiation field screening in photoconductive antennae studied via pulsed terahertz emission spectroscopy," *Appl. Phys. Lett.*, vol. 91, Dec. 2007, Art. no. 232506.
- [23] C. W. Berry and M. Jarrahi, "Principles of impedance matching in photoconductive antennas," *J. Infrared, Millimeter, THz Waves*, vol. 33, no. 12, pp. 1182–1189, Dec. 2012.
- [24] N. Khiabani, Y. Huang, Y.-C. Shen, and S. Boyes, "Theoretical modeling of a photoconductive antenna in a terahertz pulsed system," *IEEE Trans. Antennas Propag.*, vol. 61, no. 4, pp. 1538–1546, Apr. 2013.
- [25] R. Emadi, N. Barani, R. Safian, and A. Z. Nezhad, "Hybrid computational simulation and study of terahertz pulsed photoconductive antennas," *J. Infrared, Millimeter, THz Waves*, vol. 37, no. 11, pp. 1069–1085, Aug. 2016.
- [26] J. Prajapati, M. Bharadwaj, A. Chatterjee, and R. Bhattacharjee, "Circuit modeling and performance analysis of photoconductive antenna," *Opt. Commun.*, vol. 394, pp. 69–79, Jul. 2017.

- [27] I. Malhotra, P. Thakur, S. Pandit, K. R. Jha, and G. Singh, "Analytical framework of small-gap photoconductive dipole antenna using equivalent circuit model," *Opt. Quant. Electron.*, vol. 49, no. 10, Sep. 2017, Art. no. 334.
- [28] O. A. Castaneda-Urbe, C. A. Criollo, S. Winnerl, M. Helm, and A. Avila, "Comparative study of equivalent circuit models for photoconductive antennas," *Opt. Exp.*, vol. 26, no. 22, pp. 29017–29031, Oct. 2018.
- [29] G. J. Nissiyah and M. G. Madhan, "A simple equivalent circuit model of photoconductive dipole antenna for the study of terahertz intensity modulation," *Opt. Quantum Electron.*, vol. 53, no. 4, Mar. 2021, Art. no. 173.
- [30] V. Rathinasamy, R. R. Thipparaju, E. N. F. Boby, and S. Mondal, "Numerical investigation and circuit analysis of interdigitated photoconductive antenna for terahertz applications," *Opt. Quantum Electron.*, vol. 54, no. 4, Mar. 2022, Art. no. 239.
- [31] A. Garufo, G. Carluccio, N. Llombart, and A. Neto, "Norton equivalent circuit for pulsed photoconductive antennas—Part I: Theoretical model," *IEEE Trans. Antennas Propag.*, vol. 66, no. 4, pp. 1635–1645, Apr. 2018.
- [32] A. Neto, N. Llombart, and A. Freni, "Time-domain modelling of pulsed photoconducting sources—Part I: The Norton equivalent circuit," *IEEE Trans. Antennas Propag.*, vol. 71, no. 3, pp. 2527–2535, Mar. 2023.
- [33] A. F. Bernardis et al., "Time-domain modelling of pulsed photoconducting sources—Part II: Characterization of a LT GaAs bow-tie antenna," *IEEE Trans. Antennas Propag.*, vol. 71, no. 3, pp. 2536–2545, Mar. 2023.
- [34] N. Llombart and A. Neto, "THz time-domain sensing: The antenna dispersion problem and a possible solution," *IEEE Trans. THz Sci. Technol.*, vol. 2, no. 4, pp. 416–423, Jul. 2012.
- [35] V. Rumsey, "On the design and performance of feeds for correcting spherical aberration," *IEEE Trans. Antennas Propag.*, vol. 18, no. 3, pp. 343–351, May 1970.
- [36] H. Zhang, S. O. Dabironezare, G. Carluccio, A. Neto, and N. Llombart, "A Fourier optics tool to derive the plane wave spectrum of quasi-optical systems [EM programmer's notebook]," *IEEE Antennas Propag. Mag.*, vol. 63, no. 1, pp. 103–116, Feb. 2021.
- [37] TERA K15, Menlo Syst. Accessed: 2023. [Online]. Available: <https://www.menlosystems.com/products/thz-time-domain-solutions/tera15-terahertz-spectrometer>
- [38] TERA15-FC, Menlo Syst. Accessed: 2023. [Online]. Available: <https://www.menlosystems.com/de/products/thz-antennas-and-components/tera15-fc>
- [39] H. Zhang, N. Llombart, A. Freni, and A. Neto, "Frequency-domain Norton resistance for pulsed photoconductive antennas," in *Proc. Eur. Conf. Antennas Propag.*, 2023, pp. 1–6.
- [40] H. Zhang, A. Neto, J. Bueno, P. Sberna, and N. Llombart, "On the modelling of a quasi-optical link between two photoconductive antennas under pulsed laser illumination," in *Proc. Eur. Conf. Antennas Propag.*, 2022, pp. 1–2.
- [41] A. Neto, S. Monni, and F. Nennie, "UWB, non dispersive radiation from the planarly fed leaky lens antenna—Part II: Demonstrators and measurements," *IEEE Trans. Antennas Propag.*, vol. 58, no. 7, pp. 2248–2258, Jul. 2010.
- [42] E. Pancera, T. Zwick, and W. Wiesbeck, "Spherical fidelity patterns of UWB antennas," *IEEE Trans. Antennas Propag.*, vol. 59, no. 6, pp. 2111–2119, Jun. 2011.
- [43] A. Garufo et al., "Norton equivalent circuit for pulsed photoconductive antennas—Part II: Experimental validation," *IEEE Trans. Antennas Propag.*, vol. 66, no. 4, pp. 1646–1659, Apr. 2018.
- [44] H. Zhang, A. Neto, and N. Llombart, "On the modelling of the quasi-optical coupling between two photoconductive antennas under pulsed laser illumination," in *Proc. 46th Int. Conf. Infrared, Millimeter, THz Waves*, 2021, pp. 1–2.
- [45] CST Microw. Studio, Accessed on: 2022. [Online]. Available: <http://www.cst.com>
- [46] TICRA Tools GRASP, Accessed on: 2022. [Online]. Available: <https://www.ticra.com/software/grasp>
- [47] J. Bueno et al., "Fabrication and characterization of a leaky-lens photoconductive antenna on low temperature grown GaAs membranes," *IEEE Trans. THz Sci. Technol.*, vol. 13, no. 5, pp. 431–439, Sep. 2023.
- [48] A. Garufo, "Towards the engineering of pulsed photoconductive antennas," Ph.D. dissertation, Dept. Microelectronics, Delft Univ. Technol., Delft, The Netherlands, 2017.
- [49] H. Zhang, J. Bueno, P. Sberna, N. Llombart, and A. Neto, "Experimental setup for the characterization of a quasi-optical link between two pulsed photoconductive antennas," in *Proc. Eur. Conf. Antennas Propag.*, 2023, pp. 1–2.
- [50] H. Zhang, J. Bueno, P. Sberna, N. Llombart, and A. Neto, "On the experimental characterization of generated and received pulses of photoconductive antennas," in *Proc. 48th Int. Conf. Infrared, Millimeter, THz Waves*, 2023, pp. 1–2.
- [51] D. Grischkowsky, "Nonlinear generation of sub-psec pulses of THz electromagnetic radiation by optoelectronics applications to time-domain spectroscopy," in *Frontiers in Nonlinear Optics*, H. Walther, N. Koroteev, and M. O. Scully, Eds. Boca Raton, FL, USA: CRC Press, 1993.
- [52] S. S. Prabhu, S. E. Ralph, M. R. Melloch, and E. S. Harmon, "Carrier dynamics of low-temperature-grown GaAs observed via THz spectroscopy," *Appl. Phys. Lett.*, vol. 70, no. 18, pp. 2419–2421, May 1997.
- [53] M. C. Beard, G. M. Turner, and C. A. Schmuttenmaer, "Subpicosecond carrier dynamics in low-temperature grown GaAs as measured by time-resolved terahertz spectroscopy," *J. Appl. Phys.*, vol. 90, no. 12, pp. 5915–5923, Dec. 2001.
- [54] V. Ortiz, J. Nagle, J.-F. Lampin, E. Peronne, and A. Alexandrou, "Low-temperature-grown GaAs: Modeling of transient reflectivity experiments," *J. Appl. Phys.*, vol. 102, no. 4, Aug. 2007, Art. no. 043515.



Huasheng Zhang (Member, IEEE) received the B.Eng. degree (*cum laude*) in electronic information engineering from Beihang University, Beijing, China, in 2016, and the M.Sc. (*cum laude*) and Ph.D. degrees in electrical engineering from the Delft University of Technology, Delft, The Netherlands, in 2018 and 2024, respectively.

His research interests include analyzing and designing leaky-wave antennas, lens antennas, photoconductive antennas, and quasi-optical systems at millimeter and sub-millimeter wavelengths, and high-frequency electromagnetic analysis techniques.



Nuria Llombart (Fellow, IEEE) received the master's and Ph.D. degrees in electrical engineering from the Polytechnic University of Valencia, Valencia, Spain, in 2002 and 2006, respectively.

During her master's degree studies, she spent one year with the Friedrich-Alexander University of Erlangen-Nuremberg, Erlangen, Germany, and worked with the Fraunhofer Institute for Integrated Circuits, Erlangen, Germany. From 2002 to 2007, she was with Antenna Group, TNO Defense, Security and Safety Institute, The Hague, The Netherlands, working as a Ph.D. student and afterward as a Researcher. From 2007 to 2010, she was a Postdoctoral Fellow with the California Institute of Technology, Pasadena, CA, USA, working with Submillimeter Wave Advance Technology Group, Jet Propulsion Laboratory, Pasadena. She was a "Ramón y Cajal" Fellow with the Department of Optics, Complutense University of Madrid, Madrid, Spain, from 2010 to 2012. In September 2012, she joined the THz Sensing Group, Delft University of Technology, Delft, The Netherlands, where she has been a Full Professor, since February 2018. She has coauthored more than 150 journal and international conference contributions. Her research interests include the analysis and design of planar antennas, periodic structures, reflector antennas, lens antennas, and waveguide structures, with an emphasis on the THz range.

Dr. Llombart was a recipient of the H. A. Wheeler Award for the Best Applications Paper of 2008 in IEEE TRANSACTIONS ON ANTENNAS AND PROPAGATION, the 2014 THz Science and Technology Best Paper Award of the IEEE Microwave Theory and Techniques Society, the 2014 IEEE Antenna and Propagation Society Lot Shafai Mid-Career Distinguished Achievement Award, the European Research Council Starting Grant in 2015, and several NASA awards. She serves as a Board Member for the IRMMW-THz International Society.



Juan Bueno received the Graduate degree from the University of Cantabria, Santander, Spain, in 2003 and the Ph.D. degree from the University of Leiden, Leiden, The Netherlands, in 2007, both in physics.

During his Ph.D. degree studies, he studied quantum crystals at very low temperatures. From 2007 to 2008, he was a Postdoctoral Fellow with the University of California, San Diego, USA, continuing his work on quantum crystals. In 2008, he made the decision to switch research topics and interests from fundamental physics to the study of superconducting devices. He was awarded with a NASA Postdoctoral position (NPP), becoming a Postdoctor with Jet Propulsion Laboratory (JPL), USA, until 2010. During this time, he pioneered a new type of pair-breaking radiation detector, the quantum capacitance detector. After his time with JPL, he joined the Center for Astrobiology, Spain, in 2010 after receiving a JAE-doc grant, working mainly on kinetic inductance detectors (KIDs). He became an Instrument Scientist in 2012 with SRON - Netherlands Institute for Space Research, The Netherlands, working on the development of KIDs for sub-mm wave and far IR space-based observatories. He became a high-frequency RF Engineer with ELCA Group, Technical University of Delft, in 2021, working on the XG sensing and communications' laboratories. He has authored or coauthored more than 50 peer-reviewed papers, a fourth of them as the first author. His research interest concentrates on the development of over-the-air technology at sub-millimeter wave frequencies for detection and communication applications.



Angelo Freni (Senior Member, IEEE) received the Laurea (Doctors) degree in electronics engineering from the University of Florence, Florence, Italy, in 1987.

In 1994, he was involved in research with Engineering Department, University of Cambridge, Cambridge, U.K., concerning the extension and the application of the finite-element method to the electromagnetic scattering from periodic structures. From 1995 to 1999, he was an Adjunct Professor with the University of Pisa, Pisa, Italy. Between 2009 and 2010, he also spent one year as a Researcher with TNO Defence, Security, and Safety, The Hague, The Netherlands, focused on the electromagnetic modeling of kinetic inductance devices and their coupling with an array of slots in the terahertz range. Since 1990, he has been with the Department of Electronic Engineering, University of Florence, Florence, Italy, first as an Assistant Professor, and since 2002, as an Associate Professor of electromagnetism; in 2014, he obtained the Full Professor qualification. Since 2012, he has been a Visiting Professor with the TU Delft University of Technology, Delft, The Netherlands. His current research interests include meteorological radar systems, radio wave propagation, numerical and asymptotic methods in electromagnetic scattering and antenna problems, electromagnetic interaction with moving media, and remote sensing. In particular, a part of his research concerned numerical techniques based on the integral equation, with a focus on domain decomposition and fast solution methods.



Andrea Neto (Fellow, IEEE) received the Laurea degree (*summa cum laude*) in electronic engineering from the University of Florence, Florence, Italy, in 1994, and the Ph.D. degree in electromagnetics from the University of Siena, Siena, Italy, in 2000.

A part of his Ph.D. degree was developed with European Space Agency Research and Technology Center, Noordwijk, The Netherlands. He worked for the Antenna Section with European Space Agency Research and Technology Center for over two years.

From 2000 to 2001, he was a Postdoctoral Researcher with the California Institute of Technology, Pasadena, CA, USA, where he worked with the Sub-mm Wave Advanced Technology Group. From 2002 to 2010, he was a Senior Antenna Scientist with TNO Defence, Security, and Safety, The Hague, The Netherlands. In February 2010, he became a Full Professor of applied electromagnetism with the Department of Electrical Engineering, Mathematics and Computer Science, Delft University of Technology, Delft, The Netherlands, where he formed and led the THz Sensing Group. His research interests include the analysis and design of antennas with an emphasis on arrays, dielectric lens antennas, wideband antennas, EBG structures, and THz antennas.

Dr. Neto is a member of the Technical Board of the European School of Antennas and an organizer of the course on antenna imaging techniques. He is also a member of the Steering Committee of the Network of Excellence NEWFOCUS, dedicated to focusing techniques in millimeter and submillimeter wave regimes. He was a recipient of the European Research Council Starting Grant to perform research on advanced antenna architectures for THz sensing systems in 2011, the H. A. Wheeler Award for the best applications paper of 2008 in IEEE TRANSACTIONS ON ANTENNAS AND PROPAGATION, the Best Innovative Paper Prize of the 30th ESA Antenna Workshop in 2008, and the Best Antenna Theory Paper Prize of the European Conference on Antennas and Propagation in 2010. He served as an Associate Editor for IEEE TRANSACTIONS ON ANTENNAS AND PROPAGATION from 2008 to 2013 and IEEE ANTENNAS AND WIRELESS PROPAGATION LETTERS from 2005 to 2013.